

High-resolution simulations of clump-clump collisions using SPH with Particle Splitting

S. Kitsionas,^{1,2,3*} A. P. Whitworth^{3†}

¹*Astrophysikalisches Institut Potsdam, An der Sternwarte 16, D-14482, Potsdam, Germany,*

²*Institute of Astronomy & Astrophysics, National Observatory of Athens, I. Metaxa and V. Pavlou, GR-15236, P. Penteli, Greece*

³*School of Physics & Astronomy, Cardiff University, P.O. Box 913, 5 The Parade, CF24 3AA, Cardiff, U.K.*

Accepted. Received; in original form

ABSTRACT

We investigate, by means of numerical simulations, the phenomenology of star formation triggered by low-velocity collisions between low-mass molecular clumps. The simulations are performed using an SPH code which satisfies the Jeans condition by invoking On-the-Fly Particle Splitting.

Clumps are modelled as stable truncated (non-singular) isothermal, i.e. Bonnor-Ebert, spheres. Collisions are characterised by M_0 (clump mass), b (offset parameter, i.e. ratio of impact parameter to clump radius), and \mathcal{M} (Mach Number, i.e. ratio of collision velocity to effective post-shock sound speed). The gas subscribes to a barotropic equation of state, which is intended to capture (i) the scaling of pre-collision internal velocity dispersion with clump mass, (ii) post-shock radiative cooling, and (iii) adiabatic heating in optically thick protostellar fragments.

The efficiency of star formation is found to vary between 10% and 30% in the different collisions studied and it appears to increase with decreasing M_0 , and/or decreasing b , and/or increasing \mathcal{M} . For $b < 0.5$ collisions produce shock compressed layers which fragment into filaments. Protostellar objects then condense out of the filaments and accrete from them. The resulting accretion rates are high, 1 to $5 \times 10^{-5} M_{\odot} \text{ yr}^{-1}$, for the first 1 to 3×10^4 yrs. The densities in the filaments, $n_{\text{H}_2} \gtrsim 5 \times 10^5 \text{ cm}^{-3}$, are sufficient that they could be mapped in NH_3 or CS line radiation, in nearby star formation regions.

Key words: hydrodynamics – method: numerical – stars: formation – fragmentation – binaries: general – ISM: clouds

1 INTRODUCTION

There is increasing observational evidence that cloud-cloud collisions account for a substantial fraction of the star formation in the Galaxy (Scoville, Sanders & Clemens 1986; Greaves & White 1991; Hasegawa *et al.* 1994; Miyawaki, Hayashi & Hasegawa 1999; Sato *et al.* 2000). Recent theoretical calculations suggest that such collisions provide a viable mechanism for triggering star formation (Tan 2000). Cloud-cloud collisions, like all dynamical star formation mechanisms, tend to result in the formation of groups of stars.

Because the observational evidence for star formation triggered by cloud-cloud collisions comes principally from relatively violent star formation events that spawn massive OB stars, most numerical work to date has been concerned

with collisions between high-mass clouds. For example, the simulations of Chapman *et al.* (1992) treated collisions between $750 M_{\odot}$ clouds. However, if substructure in molecular clouds is hierarchical with a low volume-filling factor (Scalo 1985), one might expect a collision between two high-mass clouds to consist of many smaller-scale collisions between the lower-mass clumps of which the clouds are composed. Such a picture presupposes that the clouds and clumps are long-lived equilibrium entities. However, even in the currently most popular paradigm of clouds being transient objects formed and destroyed by turbulent motions (Padoan & Nordlund 2002; Mac Low & Klessen 2004; Bergin *et al.* 2004; Vazquez-Semadeni *et al.* 2005), fragmentation in shocks produced by large-scale converging flows can be studied in terms of smaller-scale shocks triggered by collisions between equilibrium clumps provided that such structures are of sufficiently low-mass.

The advantage of simulating collisions between lower-mass clumps is that the resolution requirements are less

* e-mail: skitsionas@aip.de

† e-mail: ant.whitworth@astro.cf.ac.uk

severe. It has been shown, both in the context of Finite Difference simulations (Truelove *et al.* 1997; Truelove *et al.* 1998), and in the context of Smoothed Particle Hydrodynamics (SPH) simulations (Bate & Burkert 1997; Kitsionas & Whitworth 2002), that gravitational fragmentation can only be modelled faithfully if the Jeans mass is resolved at all times. This requirement is normally referred to as the Jeans condition. Previous simulations of clump-clump collisions (Chapman *et al.* 1992; Pongracic *et al.* 1992; Turner *et al.* 1995; Whitworth *et al.* 1995; Bhattal *et al.* 1998; Marinho & Lépine 2000; Marinho, Andreatza & Lépine 2001) followed the evolution through several orders of magnitude in density and linear scale, and produced abundant high-mass protostellar fragments by gravitational fragmentation. However, these simulations did not satisfy the Jeans condition. Therefore, it is possible that real fragmentation on small scales was suppressed (Whitworth 1998), and/or that artificial fragmentation occurred. In this paper, we describe high-resolution simulations of clump-clump collisions, performed using SPH with On-the-Fly Particle Splitting (Kitsionas & Whitworth 2002). Particle Splitting enables us to ensure that the Jeans condition is satisfied at all times. This is achieved with relatively modest computing resources, by introducing high resolution only in the regions where it is required.

Two suites of simulations are presented aiming at i) the identification, free from numerical resolution constraints, of the dominant mechanism driving star formation in clump collisions and ii) the derivation of, at least, order of magnitude estimates for the star formation efficiency in such collisions. In the first (and principal) suite of simulations, collisions between low-mass clumps having mass $M_0 = 10M_\odot$ are simulated with various combinations of impact parameter and collision velocity. In the second suite, a few collisions between intermediate-mass clumps having $M_0 = 75M_\odot$ are simulated. The purpose of the second suite is twofold: (i) to explore the dependence on clump mass, and (ii) to repeat some of the critical simulations reported by Bhattal *et al.* (1998) and establish which of the features they inferred might be attributable to inadequate resolution.

In Section 2, we describe the physical model we use. In Section 3 we give a brief summary of our SPH code and explain how Particle Splitting is invoked to ensure the Jeans condition is always satisfied. A representative selection from the main suite of simulations (those using $10M_\odot$ clumps) is presented in Section 4. Results from the second suite ($75M_\odot$ clumps) are presented in Section 5 and compared with the results of Bhattal *et al.* (1998). In Section 6 we discuss the results and summarise our main conclusions.

2 PHYSICAL MODEL

2.1 Clump and collision parameters

In all cases, the collision involves two clumps of equal mass. In molecular clouds with hierarchical substructure, collisions between clumps at the same level of the hierarchy (i.e. with comparable mass) are the most probable (Scalo 1985) – although it would certainly be interesting to investigate collisions involving clumps of unequal mass.

The collision is set up in the centre-of-mass frame, and

so the clumps have antiparallel bulk velocities $\mathbf{v}_{\text{clump}}$ and $-\mathbf{v}_{\text{clump}}$. We define the Mach Number (\mathcal{M}) of the collision as the ratio of the relative speed of the collision ($2|\mathbf{v}_{\text{clump}}|$) to the effective post-shock sound speed (c_s , see Eqn. 1 below). We define the offset parameter b as the ratio of the impact parameter of the collision to the clump radius.

We take the clumps to be stable equilibrium isothermal spheres, i.e. they are contained by an external pressure and they are not singular (Ebert 1955; Bonnor 1956). In order to create such clumps we apply the procedure detailed in Appendix A4 of Turner *et al.* (1995). As demonstrated in Appendix B2 of Turner *et al.* (1995) this reproduces faithfully the density profile of a stable isothermal sphere, with very little particle noise.

In order to save computational time, the colliding clumps are touching when the simulations start. During the preceding approach, mutual tidal distortion should be small because the clumps move supersonically ($\mathcal{M} \gtrsim 5$). We define the x -axis to be parallel to the pre-collision velocities, and the y -axis to be parallel to the impact parameter. Hence the global angular momentum of the colliding clumps is parallel to the z -axis.

In the context of a turbulent interstellar medium, the above model can be interpreted as the interaction of flows generated at the scale of the equilibrium clumps employed here either by sources driving turbulence at these scales or by the energy cascade of turbulence driven at larger scales (Padoan & Nordlund 2002; Mac Low & Klessen 2004; Bergin *et al.* 2004; Vazquez-Semadeni, Kim & Ballesteros-Paredes 2005). The modelling of turbulent motions on smaller scales is not included self-consistently here, but rather it is represented by an isotropic pressure force in the effective sound speed (Eqn. 1) of the clumps, in accordance with the scaling relations of Larson (1981) between the internal velocity dispersion and the linear scale or the mass of a clump (e.g. see Eqn. 2). The use of an effective turbulent pressure to model turbulence acting on small scales suppresses the stochastic nature of any real density and velocity fluctuations expected from the presence of (supersonic or even transsonic) turbulent motions inside the clumps. Such an approach takes into account only the collective effect such fluctuations may have on the stability of the clump as a whole, neglecting the fact that small scale fluctuations can in turn induce collapse on these scales (Mac Low & Klessen 2004), as we mainly want to identify the role of the collision itself on the triggering of star formation.

Moreover, the current model does not take into account the effect that magnetic fields may have on the dynamics and the final outcome of the collisions. Although it is known that almost all studied clumps and cores are seen to be close to magnetic criticality (Crutcher *et al.* 2004), we effectively study here collisions between clumps threaded by weak magnetic fields, which will not become dynamically important during the course of the collisions. Given the fact that i) collisions between low-mass clumps have not been studied before and ii) the numerical methods we employ provide an adequate framework for studying self-gravitating hydrodynamics at the highest numerical resolution necessary, we believe that our assumption of magnetic subcriticality for the clumps is a reasonable first approach to this problem.

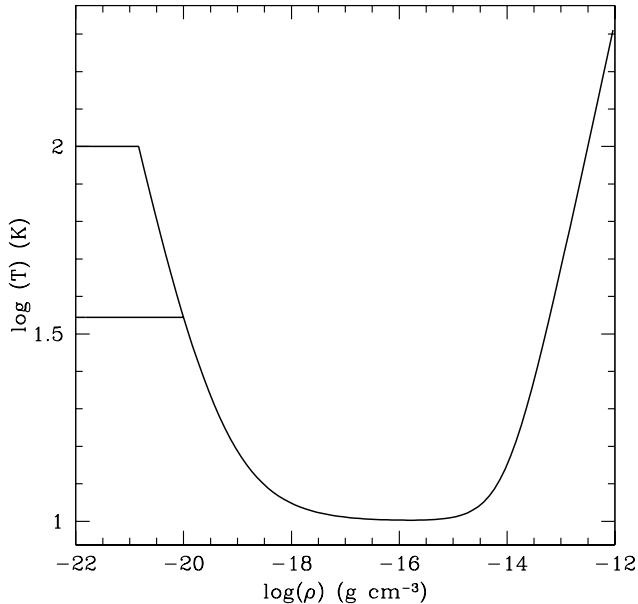


Figure 1. The equation of state given in Eqn. 1 presented as a density-temperature relation with c_0 given from Eqn. 2 for the initial clump masses adopted here (see next session), $c_s \simeq 0.2 \text{ km s}^{-1}$, $\rho_0 = \rho_c$ (ρ_c is the initial central density of a clump; see next section), $\rho_1 \simeq 10^{-14} \text{ g cm}^{-3}$. As soon as the collision starts the gas cools with $T \propto \rho^{-2/3}$ down to $T \sim 10 \text{ K}$, a temperature that is reached at $\sim 10^{-18} \text{ g cm}^{-3}$. Then it remains isothermal at $T = 10 \text{ K}$, as it is thermally coupled to the dust, until it gets optically thick to its own cooling radiation and heats up adiabatically with $T \propto \rho^{2/3}$, for densities above $10^{-14} \text{ g cm}^{-3}$.

2.2 Equation of state

We use a barotropic equation of state,

$$\frac{P}{\rho} \equiv c^2 = \begin{cases} c_0^2, & \rho \leq \rho_0; \\ [(c_0^2 - c_s^2)(\rho/\rho_0)^{-2/3} + c_s^2] \\ \quad \times [1 + (\rho/\rho_1)^{4/3}]^{1/2}, & \rho > \rho_0, \end{cases} \quad (1)$$

that is illustrated in Fig. 1. The left hand side represents the square of the effective isothermal sound speed of the gas, i.e. when non-thermal pressure due to turbulence is included.

At low densities, $\rho \leq \rho_0$ (i.e. before the collision) the clump gas has an effective sound speed

$$c_0 \sim 0.2 \text{ km s}^{-1} \left(\frac{M_0}{M_\odot} \right)^{1/4} \quad (2)$$

in accordance with Larson's scaling relation between the mass and internal velocity dispersion of a clump (Larson 1981).

Once the density exceeds $\rho_0 = \rho_c$ (ρ_c is the initial central density of a clump; see the next section for the specific values adopted here), i.e. essentially as soon as the gas is compressed by the collision shock, the gas cools down (with $T \propto \rho^{-2/3}$, see the first term on the right hand side of Eqn. 1 for $\rho > \rho_0$) to $T \sim 10 \text{ K}$ (Whitworth & Clarke 1997; Whitworth, Boffin & Francis 1998). The post-shock sound speed is therefore $c_s \simeq 0.2 \text{ km s}^{-1}$ (corresponding to a cosmic mixture of H_2 and He at 10 K). The gas reaches for the first time this temperature, and thus this sound speed,

at $\sim 10^{-18} \text{ g cm}^{-3}$ and then it evolves isothermally for a few orders of magnitude in density (see Fig. 1).

This part of the equation of state is similar to the piecewise polytropic equation of state advocated by Larson (2005). It differs mainly in the polytropic exponent assumed for the regime in which the gas is thermally coupled to the dust, i.e. above $\sim 10^{-18} \text{ g cm}^{-3}$ (Whitworth & Clarke 1997; Whitworth, Boffin & Francis 1998). For this regime, Larson's equation of state assumes slow heating of the gas ($\gamma \simeq 1.1$), whereas we have taken here the gas to evolve isothermally ($\gamma = 1$).

Finally, once the density in a collapsing protostellar object exceeds $\rho_1 \simeq 10^{-14} \text{ g cm}^{-3}$, the gas is expected to become sufficiently optically thick to its own cooling radiation that it heats up adiabatically with $T \propto \rho^{2/3}$ (Tohline 1982), given by the second term on the right hand side of Eqn. 1 for $\rho > \rho_0$. We note that for a cosmic mixture of H_2 and He at temperatures below 500 K, the adiabatic exponent is $\gamma \simeq 5/3$ because the rotational degrees of freedom of H_2 are frozen out; in our simulations the temperature does not rise above 200 K.

2.3 The two suites of collisions

A $10M_\odot$ clump has equilibrium radius $R_0 \simeq 0.22 \text{ pc}$, effective isothermal sound speed $c_0 \simeq 0.35 \text{ km s}^{-1}$ (corresponding to a cosmic mixture of H_2 and He at 35 K), central density $\rho_c \simeq 2.6 \times 10^{-20} \text{ g cm}^{-3}$ and boundary density $\rho_b \simeq 9.1 \times 10^{-21} \text{ g cm}^{-3}$. With $10M_\odot$ clumps we simulate collisions having all possible combinations of Mach Number $\mathcal{M} = 5, 10, \text{ and } 15$ (corresponding to $|\mathbf{v}_{\text{clump}}| = 0.5, 1.0 \text{ and } 1.5 \text{ km s}^{-1}$) and offset parameter $b = 0.0, 0.2, 0.4, 0.6 \text{ and } 0.8$ (the parameters adopted for each of the simulations we performed are listed in the first seven columns of Table 1). The main results of this suite of simulations are presented in Section 4.

A $75M_\odot$ clump has $R_0 \simeq 0.59 \text{ pc}$, $c_0 \simeq 0.60 \text{ km s}^{-1}$ (corresponding to a cosmic mixture of H_2 and He at $T \simeq 100 \text{ K}$), $\rho_c \simeq 1.1 \times 10^{-21} \text{ g cm}^{-3}$ and $\rho_b \simeq 3.8 \times 10^{-22} \text{ g cm}^{-3}$. With $75M_\odot$ clumps we simulate only collisions having $\mathcal{M} = 9$ and $b = 0.2, 0.4 \text{ and } 0.5$. We have chosen to study only this limited set of parameters for the intermediate-mass clump collision case, as a more detailed parameter study has been reported in Bhattal *et al.* (1998). Here we aim to verify with higher numerical resolution the validity of their conclusions on the phenomenology of clump collisions. In particular, we would like to investigate whether the existence of three distinct mechanisms of star formation, which they identified in their clump collision simulations with varying b , depends on the low numerical resolution they employed. We have therefore chosen to perform simulations with only three values of b , as according to Bhattal *et al.* (1998) collisions with $b = 0.2, 0.5 \text{ and } 0.4$ produce protostars through rotational fragmentation, filament fragmentation and the combination of the previous two, respectively. In addition, we use this suite of simulations to investigate the effect of increasing clump mass on the outcome of clump collisions (by comparing the results of this suite of simulations with those of the low-mass clump collisions with $\mathcal{M} = 10$ and corresponding values for b). The parameters adopted for each of the three intermediate-mass simulations we performed are also listed

b	\mathcal{M}	v_{coll}	v_{clump}	M_0	c_0	T	t_{frag}	M_{frag}	t_{end}	t_{evol}
0.0	5	1.0	0.5	10	0.35	35	0.472	0.33	0.476	1.08
0.2	5	1.0	0.5	10	0.35	35	0.479	0.70	0.496	1.34
0.4	5	1.0	0.5	10	0.35	35	0.535	1.11	0.557	1.44
0.6	5	1.0	0.5	10	0.35	35	0.678	0.68	0.701	1.46
0.8	5	1.0	0.5	10	0.35	35	–	–	–	–
0.0	10	2.0	1.0	10	0.35	35	0.360	0.35	0.370	1.20
0.2	10	2.0	1.0	10	0.35	35	0.360	1.00	0.396	1.72
0.4	10	2.0	1.0	10	0.35	35	0.485	0.48	0.507	1.44
0.6	10	2.0	1.0	10	0.35	35	–	–	–	–
0.8	10	2.0	1.0	10	0.35	35	–	–	–	–
0.0	15	3.0	1.5	10	0.35	35	0.320	0.47	0.332	1.24
0.2	15	3.0	1.5	10	0.35	35	0.348	0.95	0.368	1.40
0.4	15	3.0	1.5	10	0.35	35	0.433	0.31	0.453	1.40
0.6	15	3.0	1.5	10	0.35	35	–	–	–	–
0.8	15	3.0	1.5	10	0.35	35	–	–	–	–
0.2	9	1.8	0.9	75	0.60	100	0.610	0.85	0.640	1.60
0.4	9	1.8	0.9	75	0.60	100	0.660	0.40	0.686	1.52
0.5	9	1.8	0.9	75	0.60	100	0.730	0.65	0.746	1.32

Table 1. List of the initial condition parameters used for the complete set of simulations conducted in this paper (columns 1 to 7) as well as other characteristics of the evolution and final outcome of the simulations. Velocities are given in km s^{-1} , masses in M_{\odot} , temperatures in K, and times in Myr except for t_{evol} which is given in units of the $t_{\text{ff}} \sim 0.05$ Myr.

in the first seven columns of Table 1. The main results of this suite of simulations are presented in Section 5.

3 SPH WITH PARTICLE SPLITTING

3.1 Standard self-gravitating SPH

Smoothed Particle Hydrodynamics (SPH) (Gingold & Monaghan 1977; Lucy 1977; Monaghan 1992; Monaghan 2005), is a Lagrangian method for numerical hydrodynamics that assumes no symmetries or imposed grids, and is therefore very effective for treating problems that involve complex 3-dimensional geometries. SPH represents the fluid with an ensemble of \mathcal{N} discrete but extended particles. The particles are overlapping, so that all intensive quantities can be treated as continuous functions both in time and space by averaging over neighbouring particles. To implement this, a smoothing kernel with compact support is used. The smoothing kernel describes the strength and extent of a particle's influence. We use the polynomial M4 kernel (Monaghan & Lattanzio 1985).

The SPH particles move with the fluid and all hydrodynamical properties are calculated at the particle positions. To evolve the ensemble of SPH particles, we use a system of three equations, namely the continuity equation, Euler's equation and a barotropic equation of state (Eqn. 1). The SPH formulations of the first two equations, giving the density and acceleration of particle j , are

$$\rho_j = \sum_i \left\{ \frac{m_i}{h_{ij}^3} W \left(\frac{|\mathbf{r}_{ij}|}{h_{ij}} \right) \right\}, \quad (3)$$

and

$$\frac{d\mathbf{v}_j}{dt} = - \sum_i \left\{ \left[\frac{m_i}{h_{ij}^4} \left(\frac{P_i}{\rho_i^2} + \frac{P_j}{\rho_j^2} + \Pi_{ij} \right) W' \left(\frac{|\mathbf{r}_{ij}|}{h_{ij}} \right) \right. \right.$$

$$\left. \left. + \frac{m_i}{|\mathbf{r}_{ij}|^2} W^* \left(\frac{|\mathbf{r}_{ij}|}{h_{ij}} \right) \right] \frac{\mathbf{r}_{ij}}{|\mathbf{r}_{ij}|} \right\}. \quad (4)$$

Here $\mathbf{r}_{ij} = \mathbf{r}_j - \mathbf{r}_i$ and $\bar{h}_{ij} = 0.5(h_i + h_j)$. $W(s)$, $W'(s)$ and $W^*(s)$ are the kernel, its derivative ($W'(s) \equiv dW/ds$) and its volume integral (i.e. the mass fraction contained within s from the centre of the particle).

The first term on the right hand side of Eqn. 4 gives the contribution to the acceleration from hydrodynamic and artificial viscosity forces. Artificial viscosity is included to prevent particle interpenetration at shocks. We use the standard artificial viscosity (Monaghan 1992)

$$\Pi_{ij} = \begin{cases} \frac{-\alpha\mu_{ij}\bar{c}_{ij} + \beta\mu_{ij}^2}{\bar{\rho}_{ij}}, & (\mathbf{v}_{ij} \cdot \mathbf{r}_{ij}) < 0; \\ 0, & (\mathbf{v}_{ij} \cdot \mathbf{r}_{ij}) > 0, \end{cases} \quad (5)$$

where

$$\mu_{ij} = \frac{(\mathbf{v}_{ij} \cdot \mathbf{r}_{ij})\bar{h}_{ij}}{|\mathbf{r}_{ij}|^2 + 0.01\bar{h}_{ij}^2}, \quad (6)$$

$\mathbf{v}_{ij} = \mathbf{v}_j - \mathbf{v}_i$, $\bar{\rho}_{ij} = 0.5(\rho_i + \rho_j)$ and $\bar{c}_{ij} = 0.5(c_i + c_j)$ (the average isothermal sound speed). We have taken the artificial viscosity parameters to be $\alpha = \beta = 1$. A test simulation of two flows colliding at Mach Number $\mathcal{M}=10$ has shown that our code reproduces the expected density and velocity jump conditions of the shock.

The second term on the right hand side of Eqn. 4 gives the gravitational contribution to the acceleration of particle j . By using the fact that the mass of a particle is kernel smoothed, and by invoking Gauss' gravitational theorem, close gravitational interactions (that would otherwise give unphysically large accelerations) are softened. It is implicit in Eqn. 4 that we use the same smoothing length to soften both gravitational and hydrodynamical forces.

Due to the compact support of the kernel, the summations in Eqn. 3 and the first term on the right hand side of Eqn. 4 are not over all particles, but over the small number

$\mathcal{N}_{\text{neib}}$ of nearby particles for which $|\mathbf{r}_{ij}| < 2\bar{h}_{ij}$ ($\equiv h_i + h_j$). In three dimensions SPH gives good results with $\mathcal{N}_{\text{neib}} \sim 50$, and accordingly the smoothing length h_i for particle i is adjusted at each timestep so that $\mathcal{N}_{\text{neib}} \sim 50$.

Calculating the gravitational accelerations by a direct summation over all particle pairs, as implied by the right hand side of Eqn. 4, is an $\mathcal{O}(\mathcal{N}^2)$ process, and therefore prohibitively expensive for large \mathcal{N} . We avoid this expense by using the Tree-Code Gravity algorithm (Barnes & Hut 1986; Hernquist & Katz 1989), which scales as $\mathcal{O}(\mathcal{N} \log \mathcal{N})$. With this algorithm the computational domain is divided recursively into a hierarchy of cells within cells until, at the lowest level, each drawn cell contains either a single particle or no particle, from which we naturally store only tree-leaves containing a single particle each. Then we can calculate the gravitational interaction between particle j and particles at large distances from it, by treating these distant particles as a single point mass at the centre of mass of the cell to which they belong.

For the time evolution of our code we use a second order Range-Kutta integration scheme and multiple particle timesteps. A detailed description of our standard code is given in Turner *et al.* (1995).

3.2 The Jeans condition

The Jeans condition requires that the Jeans mass M_{Jeans} be resolved throughout the computational domain, at all times. In SPH, the minimum resolvable mass is estimated to be $M_{\text{resolved}} \sim \mathcal{N}_{\text{neib}} m_{\text{ptcl}}$, where m_{ptcl} is the mass of a single SPH particle (Bate & Burkert 1997). In a three-dimensionally extended medium, the Jeans mass is given by $M_{\text{Jeans}} \sim G^{-3/2} \rho^{-1/2} c^3$. Thus the Jeans condition, $M_{\text{resolved}} \lesssim M_{\text{Jeans}}$, reduces to a maximum density that can be resolved with SPH particles of mass m_{ptcl} ,

$$\rho_{\text{max}} \sim \frac{c^6}{G^3 (\mathcal{N}_{\text{neib}} m_{\text{ptcl}})^2}, \quad (7)$$

or equivalently a maximum SPH particle mass that can be used to model gas having density ρ ,

$$m_{\text{max}} \sim \frac{c^3}{G^{3/2} \rho^{1/2} \mathcal{N}_{\text{neib}}}. \quad (8)$$

With the barotropic equation of state that we are using (Eqn. 1), the combination $c^3/\rho^{1/2}$ reaches its minimum when $\rho \sim \rho_1$, i.e. when the gas switches from being approximately isothermal ($c \simeq c_s$) for $\rho_0 < \rho < \rho_1$ to approximately adiabatic for $\rho > \rho_1$. Hence, the maximum SPH particle mass becomes

$$m_{\text{max}} \sim \frac{c_s^3}{G^{3/2} \rho_1^{1/2} \mathcal{N}_{\text{neib}}} \sim 5 \times 10^{-5} M_{\odot}; \quad (9)$$

where the final evaluation has been made by substituting $c_s \sim 0.2 \text{ km s}^{-1}$, $\rho_1 \sim 10^{-14} \text{ g cm}^{-3}$, and $\mathcal{N}_{\text{neib}} \sim 50$.

A second – but as it turns out less severe – constraint on the mass of an SPH particle can be obtained by considering the shock compressed layer which forms between two colliding clumps, and requiring that the fragments into which it breaks up are resolved. Whitworth *et al.* (1994a) have shown, on the basis of linear perturbation analysis,

that these fragments should have mass

$$\begin{aligned} M_{\text{frag}} &\sim \frac{c_s^3}{(G^3 \rho_{\text{clump}} \mathcal{M})^{1/2}} \\ &\sim \left(\frac{c_s}{c_0}\right)^3 \frac{M_0}{\mathcal{M}^{1/2}} \\ &\sim \frac{M_{\odot}^{3/4} M_0^{1/4}}{\mathcal{M}^{1/2}}, \end{aligned} \quad (10)$$

where we have obtained the second expression by substituting $\rho_{\text{clump}} \sim c_0^6/G^3 M_0^2$ for the pre-collision density of a clump in hydrostatic equilibrium, and the third expression by substituting for c_0 from Eqn. 2. If we now require that $M_{\text{resolved}} \lesssim M_{\text{frag}}$, the maximum SPH particle mass becomes

$$\begin{aligned} m'_{\text{max}} &\sim \frac{M_{\odot}^{3/4} M_0^{1/4}}{\mathcal{N}_{\text{neib}} \mathcal{M}^{1/2}} \\ &\sim 2 \times 10^{-2} M_{\odot} \left(\frac{M_0}{M_{\odot}}\right)^{1/4} \mathcal{M}^{-1/2}. \end{aligned} \quad (11)$$

Unless we consider very high-velocity collisions between very low-mass clumps, m'_{max} is much larger, and therefore less restrictive, than m_{max} .

It follows that, if the Jeans condition is to be satisfied, a standard SPH code cannot model a collision between two $10M_{\odot}$ clumps with fewer than $\sim 400,000$ SPH particles, and a collision between two $75M_{\odot}$ clumps requires $\sim 3,000,000$ SPH particles. Simulations with such particle numbers are routinely performed at large parallel supercomputers (Bate, Bonnell & Bromm 2003; Bate & Bonnell 2005; Jappsen *et al.* 2005), but on the smaller serial machines available to us they are prohibitive. In order to circumvent these prohibitive computational requirements, we have applied Particle Splitting (Kitsionas & Whitworth 2002).

3.3 Particle Splitting

In Particle Splitting, we replace individual particles (parent particles) with small groups of particles (families of child particles) either globally in a predefined sub-region of the computational domain where we anticipate the need for greater resolution (*Nested Splitting*) or conditionally according to some locally defined criterion (*On-the-Fly Splitting*). Each parent particle is replaced by thirteen child particles, having masses $m_{\text{child}} = m_{\text{parent}}/13$ and smoothing lengths $h_{\text{child}} = h_{\text{parent}}/13^{1/3}$. One of these child particles is placed at the same position as its parent, and the other twelve child particles are positioned on the vertices of an hexagonal closed packed array, at equal distances $\ell = 1.5h_{\text{child}}$ from the central child particle, and from each other. The family of thirteen child particles is then rotated to an arbitrary orientation. By positioning the child particles in this way, we ensure (i) that the family of child particles is as close as possible to the spherically symmetric mass distribution of the parent particle, and (ii) that the local transient fluctuations due to Particle Splitting are minimised (Kitsionas & Whitworth 2002).

Each child particle is given a velocity $\mathbf{v}_{\text{child}}$ interpolated from the velocity field of its parent's neighbours i (including the parent j itself). This is formally given by

$$\mathbf{v}(\mathbf{r}_{\text{child}}) = \sum_{i,j} \left\{ \frac{m_i \mathbf{v}_i}{\rho_i \bar{h}_{ij}^3} W \left(\frac{|\mathbf{r}_{\text{child}} - \mathbf{r}_i|}{\bar{h}_{ij}} \right) \right\}. \quad (12)$$

The initial densities and accelerations of the child particles are then calculated using the standard SPH procedures (Eqns. 3 & 4). Subsequently, the child particles are also evolved with standard SPH procedures. The only difference is that, to mitigate interactions between adjacent particles having different masses, we have modified the scheme by which we calculate the smoothing lengths of particles. We now evolve h_i , the smoothing length for particle i , so that the radius $2h_i$ contains ~ 50 times the mass of particle i , i.e. $50 m_i$, rather than 50 other particles. This method can potentially introduce sampling errors in the calculation of the hydrodynamics quantities (see Eqn. 3 & 4), in case only a handful of neighbouring particles end up within $2h_i$, e.g. a child particle surrounded only by more massive particles. We have not addressed such special cases in our current code as corresponding tests, presented in Kitsionas (2000), have shown that such errors are negligible. However, we caution the reader that this can be a potential problem with the implementation of Particle Splitting in other SPH codes.

In Kitsionas & Whitworth (2002) we have tested On-the-Fly Splitting on the standard Boss & Bodenheimer (1979) problem. On-the-Fly Particle Splitting is invoked in response to the imminent violation of the Jeans condition, i.e. whenever the density is about to exceed ρ_{max} (Eqn. 7). SPH with Particle Splitting (either Nested or On-the-Fly) reproduces faithfully the results obtained with a standard high-resolution SPH simulation (using sufficient particles to satisfy the Jeans condition without Particle Splitting, but also using much more memory and CPU), *and* the results of high-resolution Adaptive-Mesh-Refinement Finite-Difference simulations (Truelove *et al.* 1997; Klein *et al.* 1999). It also conforms to the analytic predictions of Inutsuka & Miyama (1992).

In principle, Particle Splitting can be applied repeatedly to produce successive generations of ever smaller SPH particles, and hence ever finer mass-resolution. However, in the simulations presented here only one generation of child particles is needed. By invoking a single generation of Particle Splitting, we are able to start the simulations with SPH particles having $m_{\text{ptcl}} = 13m_{\text{max}} \simeq 6.5 \times 10^{-4} M_{\odot}$ (Eqn. 9). Therefore, initially a $10M_{\odot}$ clump can be modelled with just 15,000 particles, and a $75M_{\odot}$ clump with 110,000 particles. The critical density at which these initial particles have to be split to avoid violating the Jeans condition is

$$\rho_{\text{split}} = 13^{-2} \rho_1 \simeq 6 \times 10^{-17} \text{ g cm}^{-3}. \quad (13)$$

After this generation of Particle Splitting, adiabatic heating switches on before the simulation reaches its resolution limit again, and therefore, the Jeans condition is obeyed all the way up to the highest densities that can be achieved[‡].

[‡] The Jeans mass increases with increasing density after adiabatic heating switches on, as $M_{\text{Jeans}} \propto c_s^3 \rho^{-1/2}$ and in this regime $c_s \propto \rho^{1/3}$ (*cf.* Eqn. 1). We note that the Jeans mass increases with increasing density for all adiabatic exponents greater than 4/3.

Figure 2. Linear density profile (particle plot) of one of the protostars formed at the end of the simulation with $M_0 = 10M_{\odot}$, $b = 0.2$, $\mathcal{M} = 10$, specifically the protostar at the bottom right of both panels of Fig. 4, with diameter of $\sim 7.5 \times 10^{-4}$ pc and density contrast of ~ 3 orders of magnitude. For comparison, the solid line illustrates the density profile of a single isolated particle with mass and smoothing length corresponding to those of particles close to the peak density of the protostar.

3.4 Plots and diagnostics

We use grey-scale column density plots to present our results. All structure formed is contained within a single layer and therefore such plots are not greatly confused by projection effects. Column density plots are preferred to particle plots as the former give a more accurate representation of the total density field, and of what would be seen in optically thin molecular-line (or dust-continuum) radiation, assuming a uniform excitation temperature (or dust temperature). The figure captions give the linear size of each plot, the viewing axis, the time, and the range of the grey-scale (which is in all cases logarithmic, in units of g cm^{-2}).

In the sequel, we refer to all collapsing fragments identified in our simulations as protostars and to their discs as protostellar discs. We would like to note that the terms “protostar” and “protostellar” do not refer to pre-main-sequence (PMS) objects, as our simulations stop at much lower density than that of PMS stars. Nevertheless, we use these terms for the fragments formed in our simulations, as all such fragments appear to have the characteristics of prestellar cores, i.e. collapsing cores not associated with *IR* sources.

When a protostar forms, its linear density profile appears like a normal distribution around its peak density. At the end of our simulations, this profile is rather steep (e.g. Fig. 2). To infer its mass, we take the protostar to extend out to $d_i = 3\sigma_i$, where σ_i is the FWHM in each of the three Cartesian axes $i = x, y, z$, and we sum the masses of the SPH particles that lie within all three diameters d_i . The radius of the protostar is given by the largest of the three radii $r_i = d_i/2$. This method gives good results for the mass and the radius of spherical as well as disc-like protostars.

In essence, our method is similar to the Stutzki & Güsten (1990) clump-finding technique. Nevertheless, because of the low number of protostars formed in our simulations, we need not subtract each protostar from the density field before searching for the next one in the residuals. Therefore, we apply our method simultaneously to all protostars that are identified by eye in our simulations[§]. Moreover, we note that, when applied to a few of our simulations, the Williams *et al.* (1994) clump-finding algorithm, as implemented for SPH by Klessen & Burkert (2000), gives results very similar to those of our method. In Table 1, we list the total mass of fragments, M_{frag} , at the end of each simulation.

Because our simulations evolve at very high resolution and due to the Lagrangian nature of SPH, the timestep becomes extremely small in the densest parts of the computational domain, i.e. within the protostellar fragments formed. As a result, after a few thousand timesteps our simulations approach a state of suspended animation, when the very small particle distances within the fragments dominate the system evolution. We have arbitrarily chosen to terminate all simulations after 10,000 timesteps as it becomes extremely inefficient computationally to continue any further. To demonstrate that this is a reasonable choice, we have continued one of the simulations for another 10,000 timesteps, during which the simulation advanced in physical time by only an additional $\sim 1\%$.

4 $10M_{\odot}$ CLUMP COLLISIONS

In these simulations the colliding clumps each have mass $M_0 = 10M_{\odot}$, radius $R_0 \simeq 0.22$ pc, and pre-collision effective sound speed $c_0 \simeq 0.35$ km s⁻¹. In the centre-of-mass frame, their velocities are $\mathbf{v}_{\text{clump}}$ and $-\mathbf{v}_{\text{clump}}$ and they collide with impact parameter bR_0 . We simulate collisions with Mach Numbers $\mathcal{M} = 5, 10, 15$ (corresponding to $|\mathbf{v}_{\text{clump}}| \simeq 0.5, 1.0, 1.5$ km s⁻¹), and $b = 0, 0.2, 0.4, 0.6, 0.8$ (corresponding to impact parameters 0, 0.044, 0.088, 0.132, 0.176 pc).

Table 2 summarises the main results of all low-mass collision simulations performed. In the following subsections we describe in more detail a subset of the simulations. First we hold $b = 0.2$ (constant) and increase \mathcal{M} through $\mathcal{M} = 5$ (§4.2), $\mathcal{M} = 10$ (§4.3), and $\mathcal{M} = 15$ (§4.4); then we hold $\mathcal{M} = 5$ (constant) and increase b through $b = 0.2$ (§4.2), $b = 0.4$ (§4.5), and $b = 0.6$ (§4.6). In the following subsection we give a short overview of the expected outcome of clump collisions as discussed in Whitworth *et al.* (1994a; 1994b).

4.1 Analysis

The outcome of a collision between clumps can be analysed in terms of three factors, namely (i) the mass, extent and lifetime of the shock compressed layer, (ii) the fragmentation scale in the shock compressed layer, and (iii) the net angular momentum of the shock compressed layer.

(i) *The mass, extent and lifetime of the shock compressed layer.* For a given clump mass M_0 , the amount of mass which is shock compressed depends on the impact parameter. Evidently it is a maximum for head-on collisions ($b = 0$), and decreases monotonically with increasing b , becoming negligible for $b \gtrsim 0.6$. For larger impact parameter, two further factors come into play. Firstly, the mass of the shock compressed layer is increased somewhat at low Mach Number because the clump trajectories are focused by their mutual gravitational attraction. The escape speed from the surface of a clump, $v_{\text{esc}} = (2GM_0/R_0)^{1/2}$, is ~ 0.6 km s⁻¹ for a $10M_{\odot}$ clump, and so focusing is only important for the collisions with $|\mathbf{v}_{\text{clump}}| \sim 0.5$ km s⁻¹ (i.e. $\mathcal{M} = 5$). Secondly, at high impact parameter and high Mach Number, a shock compressed layer forms but is then torn apart by shear before it can fragment.

(ii) *The fragmentation scale in the shock compressed layer.* As discussed in Whitworth *et al.* (1994a; 1994b), the preferred fragment mass in a shock compressed layer is given by Eqn. 10, and the fragmentation scale (i.e. the mean separation between fragments, in the plane of the shock compressed layer) is

$$\begin{aligned} L_{\text{frag}} &\sim \frac{c_s}{(G\rho_{\text{clump}}\mathcal{M})^{1/2}} \\ &\sim \left(\frac{c_s}{c_0}\right) \frac{R_0}{\mathcal{M}^{1/2}} \\ &\sim \left(\frac{M_0}{M_{\odot}}\right)^{-1/4} \frac{R_0}{\mathcal{M}^{1/2}}. \end{aligned} \quad (14)$$

We have obtained the second expression by substituting $\rho_{\text{clump}} \sim c_0^6/G^3M_0^2$ for the pre-collision density of a clump in hydrostatic equilibrium and $R_0 \sim GM_0/c_0^2$ for its radius, and the third expression by substituting for c_0 from Eqn. 2. It follows that for given clump mass M_0 and given (low) offset parameter b , increasing the Mach Number of the collision will decrease L_{frag} , and hence increase the number of filaments into which the shock compressed layer fragments, and the number of protostars. At large b , the fragmentation scale is increased somewhat by the shear in the shock compressed layer. However, this effect is only significant for $b \gtrsim 0.5$, and the mass of the shock compressed layer is then negligible.

We should stress that the fragmentation of a shock compressed layer is essentially a two-dimensional process, initially. The fragmentation scale L_{frag} defines the size of proto-condensations in the plane of the layer. The thickness of the layer is much smaller than L_{frag} . The number of filaments and protostars is therefore determined by the ratio of the lateral extent of the shock compressed layer to the fragmentation scale.

(iii) *The net angular momentum of the shock compressed layer.* The net angular momentum of the shock compressed layer increases with increasing impact parameter and increasing collision velocity, i.e. increasing b and \mathcal{M} . Increased angular momentum means that the ensemble of protostars has more collective orbital angular momentum, and so mergers between protostars are less likely. Additionally, it means that the material which accretes onto the individual protostellar discs from the filaments has higher specific angular momentum, and therefore spins them up more rapidly.

[§] A protostar is identified for the first time when its peak density exceeds ~ 100 times the density of its surroundings. We consider this time of first identification as the formation time of the protostar.

$\mathcal{M} \setminus b$	0.0	0.2	0.4	0.6
5	One spherical rotating object. $0.33M_{\odot}$. No filaments.	One disc-like object. $0.7M_{\odot}$. Spiral arms. No companions. A single filament.	Two disc-like objects. $1.11M_{\odot}$ in total. Only most massive with spiral arms. Possible companions. Single filament.	Two well-separated rotating objects. $0.68M_{\odot}$ in total. Only most massive with spiral arms. Possible companions. No filaments.
10	One spherical rotating object. $0.35M_{\odot}$. Two filaments.	Two disc-like objects (+ a third forming). $1.0M_{\odot}$ in total. Both spiral arms. No companions. Network of filaments.	Single disc-like object (+ a second forming). $0.48M_{\odot}$. Spiral arms. Possible companions. Single filament.	No shock.
15	One disc-like rotating object. $0.47M_{\odot}$. No spiral arms. Network of filaments.	Two disc-like objects (+ a third forming). $0.95M_{\odot}$ in total. Only most massive with spiral arms. Possible companions. Well-defined network of filaments.	Single disc-like object. $0.31M_{\odot}$. Spiral arms. No companions. No filaments.	No shock.

Table 2. Summary of simulations and most important results for the low-mass clump collisions ($M_0 = 10M_{\odot}$) for the different values of b and \mathcal{M} . Shocks do not form in any of the $b = 0.8$ runs.

In the following five subsections we describe five simulations which illustrate the above features of collisions between $10M_{\odot}$ clumps.

4.2 $M_0 = 10M_{\odot}$, $b = 0.2$, $\mathcal{M} = 5$

The initial conditions are shown in the left panel of Fig. 3. On-the-Fly Particle Splitting starts at $t_{\text{split}} \sim 0.463$ Myr. A single tumbling filament forms at ~ 0.479 Myr, and material from the filament accretes onto a single central primary protostar[¶]. The filament is tumbling because the shock compressed layer from which it forms is tumbling, due to the orbital angular momentum in a clump-clump collision at finite impact parameter. The steadily increasing specific angular momentum of the material accreting onto the protostar from the filament creates an accretion disc around the protostar, and spiral arms develop in this disc. We are unable to follow the simulation for long enough to determine whether these arms become sufficiently self-gravitating to condense out as secondary companions.

At the end of the simulation (~ 0.496 Myr; right panel of Fig. 3), the mass of the protostar is $\sim 0.70M_{\odot}$ and its radius is ~ 90 AU. Its central density exceeds ρ_1 , which implies that it has started to heat up adiabatically. The number of active particles has increased from 30,000 to 55,300.

4.3 $M_0 = 10M_{\odot}$, $b = 0.2$, $\mathcal{M} = 10$

The initial conditions are again as in the left panel of Fig. 3. On-the-Fly Particle Splitting starts at $t_{\text{split}} \sim 0.339$ Myr. By this stage, a network of tumbling filaments has started to form. At ~ 0.360 Myr, two protostars condense out of the filaments. The protostars are rapidly rotating, and accretion discs form around them shortly after their formation. The discs are approaching each other, and depending on their

separation and their mutual alignment at periastron they are likely either to be captured into a binary, or to merge. There may be a third protostar starting to form a few timesteps before the end of the simulation.

At the end of the simulation (~ 0.396 Myr; Fig. 4), the two protostellar discs have developed strong spiral arms, but they have not yet shown any inclination to fragment. The total mass of the two protostars is $\sim 1.0M_{\odot}$. The more massive protostar has mass $0.59M_{\odot}$ and radius ~ 76 AU. The less massive protostar has mass $0.41M_{\odot}$ and radius ~ 103 AU. Their central densities exceed ρ_1 , so they have started to heat up adiabatically. The minimum density in the filaments is $\rho_{\text{fil}} \sim 2.8 \times 10^{-17} \text{ g cm}^{-3}$ ($n_{\text{H}_2} \sim 5 \times 10^6 \text{ cm}^{-3}$). The number of active particles has increased from 30,000 to 64,300.

4.4 $M_0 = 10M_{\odot}$, $b = 0.2$, $\mathcal{M} = 15$

Again, the initial conditions are as in the left panel of Fig. 3. A network of tumbling filaments forms at ~ 0.306 Myr. When compared with the filaments formed in the previous lower-velocity ($\mathcal{M} = 10$) collision, the filaments of the $\mathcal{M} = 15$ collision are better defined, and they form on the whole surface of the shock compressed layer, not just at its centre. On-the-Fly Particle Splitting starts at $t_{\text{split}} \sim 0.336$ Myr. Two protostars condense out of the central filament at ~ 0.348 Myr. These protostars are rapidly rotating, and accretion discs form around them shortly after their formation. The disc of the more massive (primary) protostar develops strong spiral arms. There are density enhancements at the points where the accretion flows intercept the spiral arms (right panel of Fig. 5). These density enhancements may subsequently become self-gravitating and condense out as secondary companions to the primary. There may be a third object starting to condense out in one of the other filaments.

At the end of the simulation (~ 0.368 Myr; Fig. 5), the total mass of the two protostars is $\sim 0.95M_{\odot}$. There is also another $\sim 0.1M_{\odot}$ associated with the spiral arms. The more massive protostar has mass $0.53M_{\odot}$ and radius ~ 42 AU.

[¶] We refer to protostars which form directly from the fragmentation of filaments as primary protostars.

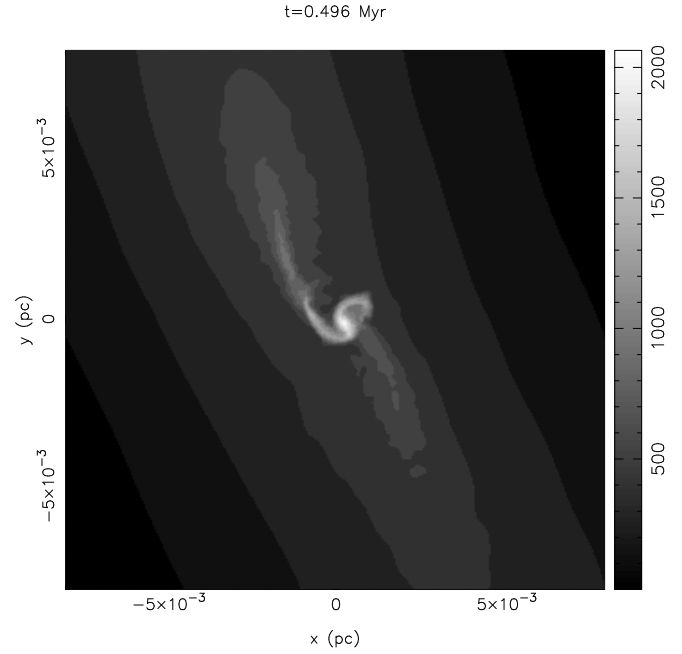


Figure 3. Column density plots for $M_0 = 10M_\odot$, $b = 0.2$, $\mathcal{M} = 5$. *Left Panel.* Initial conditions viewed along the z -axis; $\Delta x = 0.92$ pc, $\Delta y = 0.56$ pc; the grey-scale is logarithmic, in units of g cm^{-2} , with sixteen equal intervals from $1.00 \times 10^{-3} \text{ g cm}^{-2}$ to $2.69 \times 10^{-2} \text{ g cm}^{-2}$ (or equivalently, adopting solar composition, $2.50 \times 10^{20} \text{ H}_2 \text{ cm}^{-2}$ to $6.73 \times 10^{21} \text{ H}_2 \text{ cm}^{-2}$). *Right Panel.* The end of the simulation ($t = 0.496$ Myr) viewed along the z -axis; $\Delta x = \Delta y = 0.016$ pc; sixteen-interval logarithmic grey-scale, in units of g cm^{-2} , from $2.40 \times 10^{-1} \text{ g cm}^{-2}$ to $2.04 \times 10^3 \text{ g cm}^{-2}$ ($6.00 \times 10^{22} \text{ H}_2 \text{ cm}^{-2}$ to $5.10 \times 10^{26} \text{ H}_2 \text{ cm}^{-2}$).

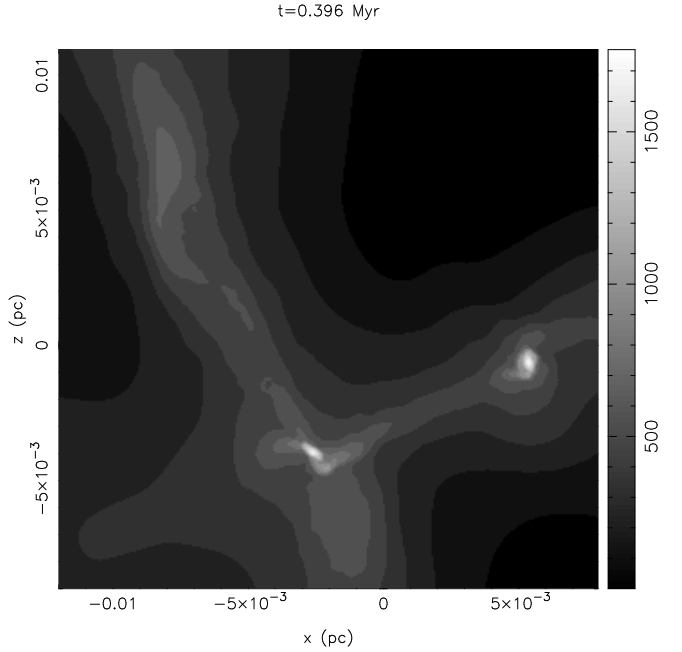


Figure 4. $M_0 = 10M_\odot$, $b = 0.2$, $\mathcal{M} = 10$ at the end of the simulation ($t \sim 0.396$ Myr). *Left Panel.* View along the z -axis; $\Delta x = 0.016$ pc, $\Delta y = 0.014$ pc; sixteen-interval logarithmic grey-scale, in units of g cm^{-2} , from $2.14 \times 10^{-1} \text{ g cm}^{-2}$ to $3.55 \times 10^3 \text{ g cm}^{-2}$ ($5.35 \times 10^{22} \text{ H}_2 \text{ cm}^{-2}$ to $8.88 \times 10^{26} \text{ H}_2 \text{ cm}^{-2}$). *Right Panel.* View along the y -axis; $\Delta x = \Delta z = 0.02$ pc; sixteen-interval logarithmic grey-scale, in units of g cm^{-2} , from $1.05 \times 10^{-1} \text{ g cm}^{-2}$ to $1.78 \times 10^3 \text{ g cm}^{-2}$ ($2.63 \times 10^{22} \text{ H}_2 \text{ cm}^{-2}$ to $4.45 \times 10^{26} \text{ H}_2 \text{ cm}^{-2}$).

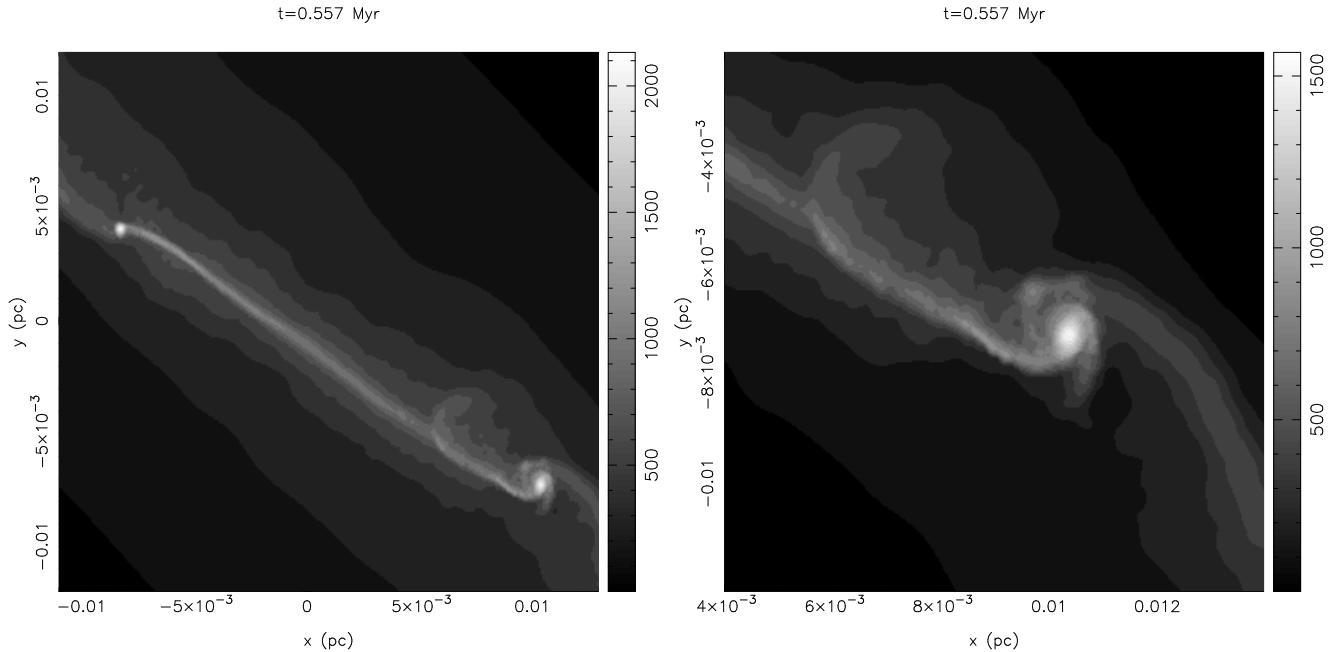


Figure 6. $M_0 = 10M_\odot$, $b = 0.4$, $\mathcal{M} = 5$ at the end of the simulation ($t = 0.557$ Myr), viewed along the z -axis. *Left Panel.* $\Delta x = \Delta y = 0.024$ pc; sixteen-interval logarithmic grey-scale, in units of g cm^{-2} , from $8.13 \times 10^{-2} \text{ g cm}^{-2}$ to $2.14 \times 10^3 \text{ g cm}^{-2}$ ($2.03 \times 10^{22} \text{ H}_2 \text{ cm}^{-2}$ to $5.35 \times 10^{26} \text{ H}_2 \text{ cm}^{-2}$). *Right Panel.* Zooming in on the protostar in the bottom right hand corner of the left panel. $\Delta x = \Delta y = 0.01$ pc.; sixteen-interval logarithmic grey-scale, in units of g cm^{-2} , from $2.24 \times 10^{-1} \text{ g cm}^{-2}$ to $1.58 \times 10^3 \text{ g cm}^{-2}$ ($5.60 \times 10^{22} \text{ H}_2 \text{ cm}^{-2}$ to $3.95 \times 10^{26} \text{ H}_2 \text{ cm}^{-2}$).

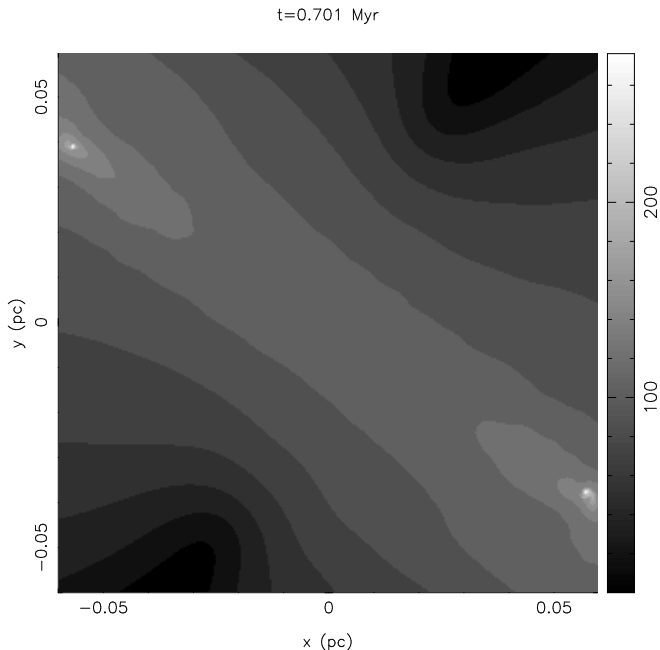


Figure 7. $M_0 = 10M_\odot$, $b = 0.6$, $\mathcal{M} = 5$, at the end of the simulation ($t = 0.701$ Myr), viewed along the z -axis; $\Delta x = \Delta y = 0.12$ pc; sixteen-interval logarithmic grey-scale, in units of g cm^{-2} , from $2.45 \times 10^{-4} \text{ g cm}^{-2}$ to $2.75 \times 10^2 \text{ g cm}^{-2}$ ($6.13 \times 10^{19} \text{ H}_2 \text{ cm}^{-2}$ to $6.88 \times 10^{25} \text{ H}_2 \text{ cm}^{-2}$).

protostars are formed – and indeed for $b \gtrsim 0.6$ no protostars are formed. Secondly, the pattern of fragmentation changes, in the sense that for higher impact parameter i) two protostars form but with one being mainly material from one clump, and the other mainly material from the other clump; ii) the two protostars thus formed are not bound to one another. Fig. 8 summarises the above main conclusions.

Accretion rates onto the protostars are typically 1 to $5 \times 10^{-5} M_\odot \text{ yr}^{-1}$. There is no obvious dependence of the accretion rate on the collision parameters.

As we discussed in Section 2.2, the gas that gets compressed in the shock at the collision interface cools radiatively down to ~ 10 K and then remains isothermal for a few orders of magnitude in density before it gets heated adiabatically. Since gas fragmentation occurs in this isothermal regime, we consider the free-fall time, t_{ff} , i.e. the most commonly used measure of the fragmentation time-scale, to be that corresponding to gas of density 1 to $2 \times 10^{-18} \text{ g cm}^{-3}$, i.e the density at which gas reaches the isothermal temperature of 10 K for the first time (*cf.* Fig. 1). This gives $t_{\text{ff}} \sim 0.05$ Myr. Indeed, the time of fragmentation, t_{frag} (which is identical to the protostar formation time according to the definition given in Section 3.4), is in all simulations delayed by approximately one t_{ff} with respect to the time at which the gas in the simulation reached, for the first time, a density of $\sim 10^{-18} \text{ g cm}^{-3}$. This means that there are two main phases of evolution in the simulations: in the first phase the dense shock compressed layer is forming (while the gas is cooling) and in the second (isothermal) phase the gas in this layer fragments. In Table 1, we list the fragmentation and the final time of each simulation, t_{frag} and t_{end} respectively

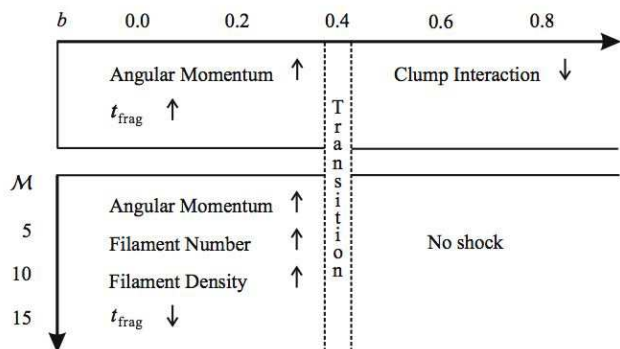


Figure 8. Dependence of different quantities and phenomena on the increasing values of b and \mathcal{M} for simulations of clump-clump collisions. Upward and downward pointing arrows indicate increasing and decreasing quantities, respectively. Note that the parameter space is divided in two sections: low- b collisions produce stronger shocks. Large- b collisions reduce the clump interaction. The transition happens at $b=0.4$.

(both given in Myr), as well as the approximate duration of the second of the two phases defined above, which we call t_{evol} (given in units of the t_{ff}), for which we have concluded that all collisions fragment *exactly* one $t_{\text{ff}} \sim 0.05$ Myr after the gas reached a temperature of 10 K for the first time.

As can be seen from Table 1, the fragmentation time, t_{frag} , decreases with increasing Mach Number, \mathcal{M} , and decreasing offset parameter, b , as the formation of the shock compressed layer progresses faster with increasing clump velocity as well as in collisions where the clumps collide closer to head-on.

In fact, the shock compressed layer breaks first into filaments which subsequently fragment to produce the (primary) protostars. Fragmentation of the filaments is, therefore, the main star formation mechanism at play in these low-mass clump collisions. It is the combination of gas cooling and self-gravity that are responsible for this behaviour. In particular, when we repeated the simulation with $b = 0.2$, $\mathcal{M} = 10$ without taking into account the gas self-gravity, the two clumps quickly passed through each other as the shock compressed layer never became sufficiently dense (only by a factor of ~ 2.5 orders of magnitude) to break up into filaments and/or protostars. Repeating the same simulation, this time including the gas self-gravity but not allowing for gas cooling (i.e. the gas was isothermal at 35 K), no shock compressed layer formed but instead a single very massive ($\gtrsim 2.5M_{\odot}$) and highly bound object formed, which was rotating very fast and was attended by a disc with spiral arms.

As can be seen from Tables 1 & 2, our simulations end at a stage when only about 1-5% of the total available gas mass has turned into protostars. Taking this value as a lower limit for the star formation efficiency (SFE) of the clump-

clump collisions we model, we can also estimate an SFE upper limit from the gas mass that ends up gravitationally bound in the filaments. This gives a value of ~ 30 -35% (e.g. for the $b = 0.2$, $\mathcal{M} = 10$ run the bound mass in the filaments is $\sim 6.7M_{\odot}$). The early termination of the simulations does not allow us to measure the SFE in a more precise way than these estimated upper and lower limits. One can also use the fact that the protostars formed here show high mass accretion rates, characteristic of Class 0 objects, and estimate an expected final mass for the protostars ~ 1 Myr after their formation (using mass accretion rates lower by one or two orders of magnitude for the duration of the Class I phase^{||}). In this way one ends up with a final mass of $1-2M_{\odot}$ per primary protostar formed. Using also the fact that 1-2 primary protostars form on average in our simulations^{**}, we infer a SFE of order 10-20% for the low-mass collisions. Based on the number of Jeans masses in the filaments, we expect that in the high \mathcal{M} , $b = 0.2$ collisions a third primary protostar will also form, as the number of Jeans masses in the filaments at the end of these collisions is of order 3. Thus, we expect the SFE of such collisions to be higher than the average, but still in the 10-20% range.

In some of our simulations, spiral arms form in the protostellar discs and we find some evidence for interactions between the spiral arms and the accretion flows. However, our simulations stop at an early stage of the disc evolution due to timestep constraints. Thus, we can not confirm that such interactions are efficient in forming companions to the protostars. Formation of secondaries by accretion-induced rotational instabilities and/or disc-disc interactions would increase the SFE. We note, however, that the Toomre q parameter^{††} for most of the discs (e.g. both discs of the $b = 0.2$, $\mathcal{M} = 10$ collision; see Fig. 4) is steadily decreasing and it is $q \gtrsim 1$ at the end of the simulations.

4.8 Repeating the $M_0 = 10M_{\odot}$, $b = 0.2$, $\mathcal{M} = 10$ simulation with sink particles

4.8.1 The algorithm and sink parameters

In order to derive a more direct estimate of the number and the final mass of the protostars that form in such collisions, we have repeated the $b = 0.2$, $\mathcal{M} = 10$ collision this time including sink particles (Bate, Bonnell & Price 1995). In particular, if certain conditions are satisfied (protostellar peak density exceeding a certain density threshold while the protostar is gravitationally bound; for details see below), we force all gas particles within a protostar to be removed from the simulation and replaced with a single collisionless (star) sink particle having as mass the sum of the masses of the

^{||} We assume, very crudely, that the Class 0 phase lasts for ~ 0.1 Myr and the Class I phase for ~ 1 Myr, after which the mass accretion rate becomes negligible.

^{**} The number of Jeans masses in the filaments is on average of order 2 at the end of the simulations.

^{††} To calculate q , we use the average values of the sound speed, density, velocity, distance from the disc centre, and distance from the disc midplane for all particles in a disc.

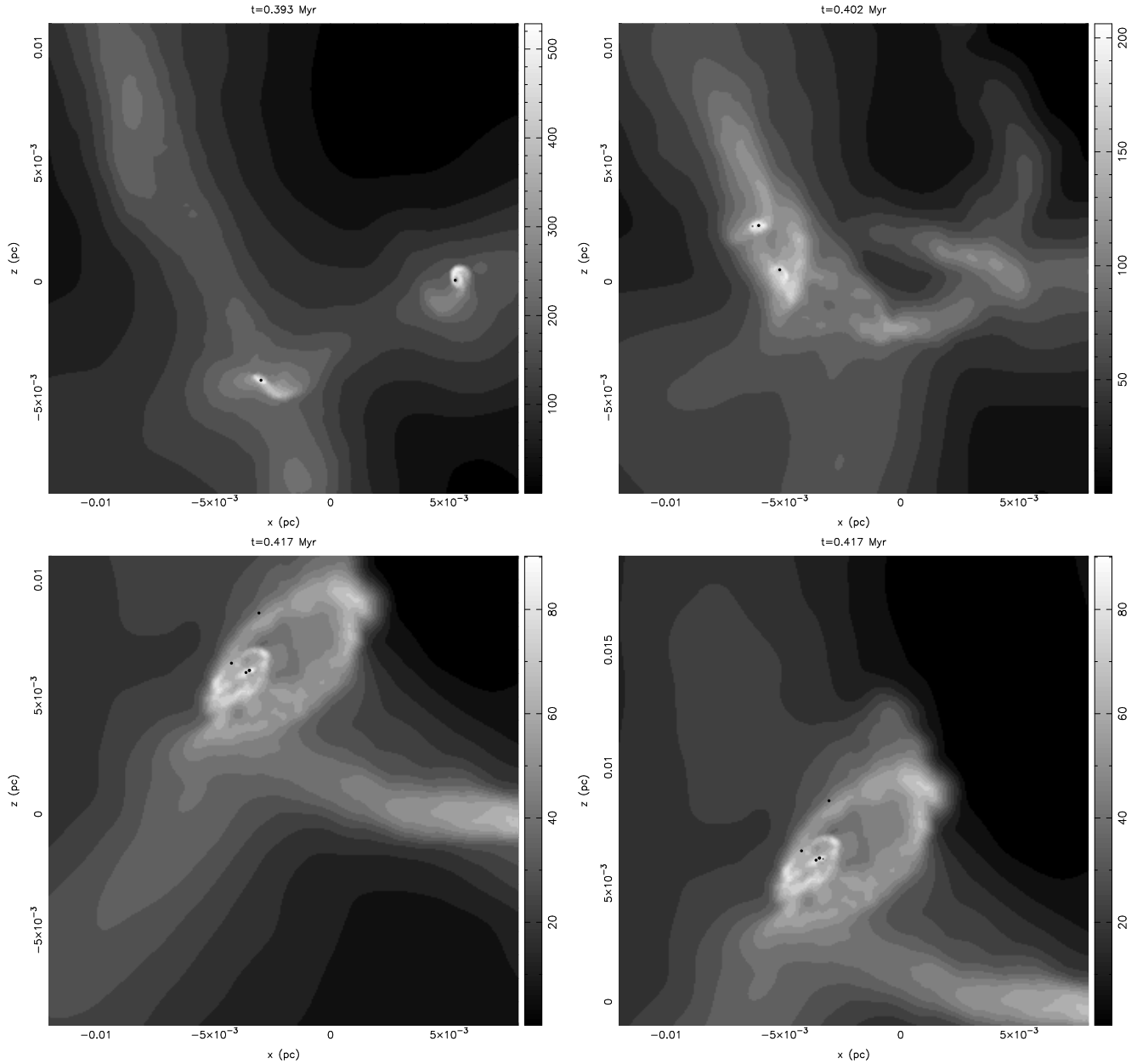


Figure 9. Continuing the $M_0 = 10M_\odot$, $b = 0.2$ $\mathcal{M} = 10$ simulation by using sink particles (overlaid solid circles; note that the symbol used for the sinks is larger than the actual sink radius at the scale of these plots). View along the y -axis; $\Delta x = \Delta z = 0.02$ pc in all panels. *Upper Left Panel.* $t \sim 0.393$ Myr, i.e. comparable to the right panel of Fig. 4 (the end of the corresponding simulation *without* sinks); sixteen-interval logarithmic grey-scale, in units of g cm^{-2} , from $3.31 \times 10^{-1} \text{ g cm}^{-2}$ to $5.25 \times 10^2 \text{ g cm}^{-2}$ ($8.28 \times 10^{22} \text{ H}_2 \text{ cm}^{-2}$ to $1.31 \times 10^{26} \text{ H}_2 \text{ cm}^{-2}$). *Upper Right Panel.* $t \sim 0.402$ Myr; sixteen-interval logarithmic grey-scale, in units of g cm^{-2} , from $2.88 \times 10^{-1} \text{ g cm}^{-2}$ to $2.04 \times 10^2 \text{ g cm}^{-2}$ ($7.20 \times 10^{22} \text{ H}_2 \text{ cm}^{-2}$ to $5.10 \times 10^{25} \text{ H}_2 \text{ cm}^{-2}$). *Both Lower Panels.* $t \sim 0.417$ Myr; the *Bottom Right Panel* is an exact copy of the *Bottom Left Panel* after having shifted the latter by 0.008 pc along the z -axis (in order to allow for direct comparisons with the corresponding plots of Fig. 10); sixteen-interval logarithmic grey-scale, in units of g cm^{-2} , from $2.45 \times 10^{-1} \text{ g cm}^{-2}$ to $9.12 \times 10^1 \text{ g cm}^{-2}$ ($6.13 \times 10^{22} \text{ H}_2 \text{ cm}^{-2}$ to $2.28 \times 10^{25} \text{ H}_2 \text{ cm}^{-2}$).

gas particles it replaces^{††}. The position and the velocity of a sink are given by mass-weighted sums of the positions and

the velocities, respectively, of the gas particles that the sink replaces. Subsequent to their formation, sinks are allowed to accrete more gas that enters their radius of influence,

^{††} It is essential to introduce sinks automatically in the simulations, as the replacement by hand of protostars with sinks will lead the system to a new state of suspended animation as soon

as another protostar forms, in which case we will have to replace this new protostar with another sink and so on.

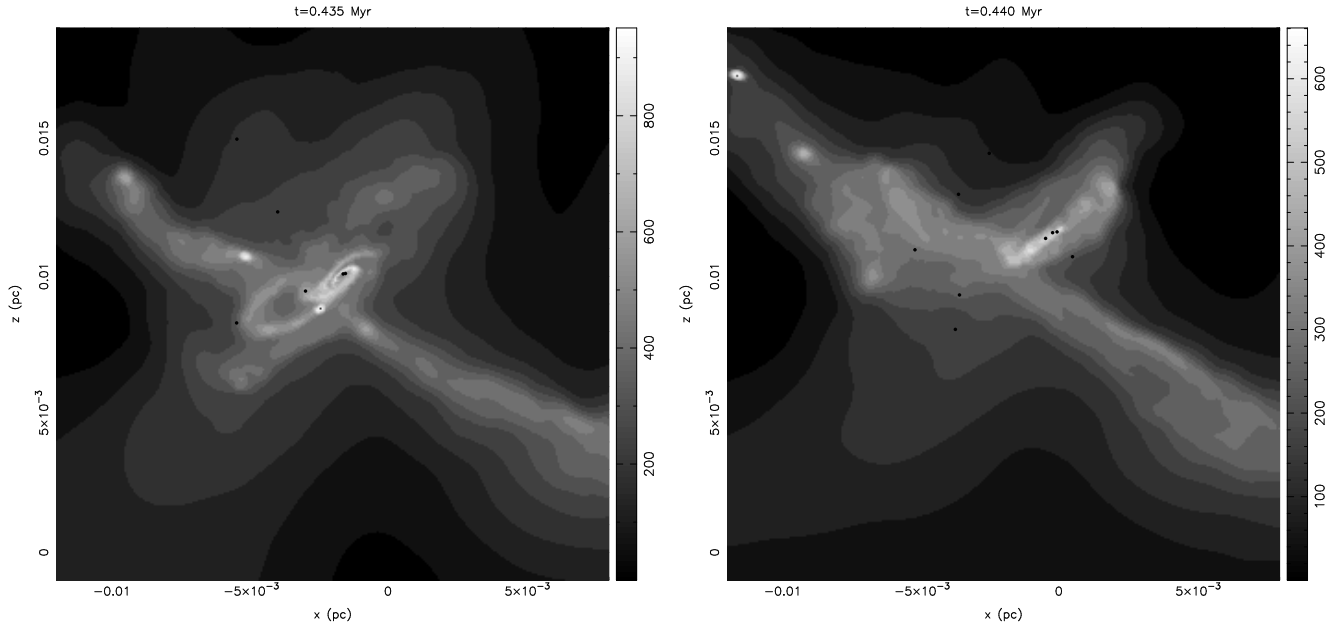


Figure 10. Continuing the $M_0 = 10M_\odot$, $b = 0.2$ $\mathcal{M} = 10$ simulation by using sink particles (overlaid solid circles; note that the symbol used for the sinks is larger than the actual sink radius at the scale of these plots). View along the y -axis; $\Delta x = \Delta z = 0.02$ pc in both panels (to be compared directly with the bottom right panel of Fig. 9). *Left Panel.* $t \sim 0.435$ Myr; sixteen-interval logarithmic grey-scale, in units of g cm^{-2} , from $3.09 \times 10^{-1} \text{ g cm}^{-2}$ to $9.55 \times 10^2 \text{ g cm}^{-2}$ ($7.73 \times 10^{22} \text{ H}_2 \text{ cm}^{-2}$ to $2.39 \times 10^{26} \text{ H}_2 \text{ cm}^{-2}$). *Right Panel.* At the end of the simulation ($t \sim 0.440$ Myr); sixteen-interval logarithmic grey-scale, in units of g cm^{-2} , from $3.39 \times 10^{-1} \text{ g cm}^{-2}$ to $6.61 \times 10^2 \text{ g cm}^{-2}$ ($8.48 \times 10^{22} \text{ H}_2 \text{ cm}^{-2}$ to $1.65 \times 10^{26} \text{ H}_2 \text{ cm}^{-2}$).

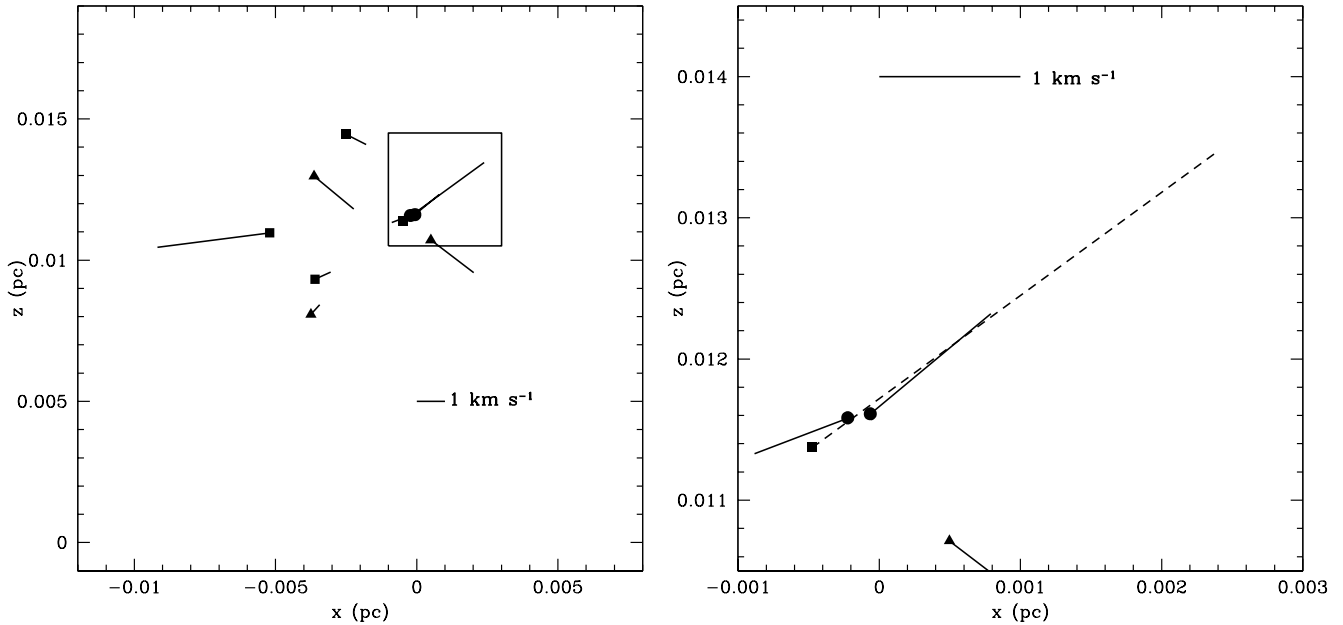


Figure 11. *Left Panel.* The positions and velocities of the 9 sinks shown in the right panel of Fig. 10, i.e. at the end of the simulation with sinks. Circles denote the binary components ($M > 1M_\odot$), squares denote low-mass protostars ($0.1M_\odot < M < 1M_\odot$) and triangles denote protostars in the sub-stellar mass range ($M < 0.1M_\odot$). The lines indicate the projection of the velocity of each sink on the xz -plane using a scaling of $1000 \text{ km s}^{-1} : 1 \text{ pc}$. A 1 km s^{-1} velocity line is indicated for clarity at the bottom of this panel. The direction of each velocity vector is pointing *away* from the corresponding symbols. *Right Panel.* Zooming in close to the binary (the region enclosed by the square in the left panel). For clarity the velocity of the low-mass companion of the binary is illustrated by a dashed line. The 1 km s^{-1} velocity line is indicated at the top of this panel.

r_{sink} . This is the only way the sinks interact with the gas, apart from the boundary conditions that they impose on their neighbouring gas particles (see the discussion below). Gas particles that are accreted by a sink are removed from the simulation. The sinks are subject only to the force of gravity, exchanging gravitational interactions with all types of particles. Sink-sink interactions are Plummer softened at distances smaller than $2 \times r_{\text{sink}}$.

The conditions for sink creation are that a protostar is i) dense enough, i.e. its peak density exceeds a certain threshold, specifically $\rho_{\text{sink}} = 10^{-12} \text{ g cm}^{-3}$, which is 100 times higher than ρ_1 , the density after which adiabatic heating switches on; and ii) gravitationally bound, i.e. the gas within the protostar has already started collapsing. In terms of the Jeans analysis, from the second of the above sink formation conditions we obtain the minimum mass of a sink that can be resolved at ρ_{sink} as well as the corresponding sink creation radius which also serves as the sink accretion radius, r_{sink} . In particular, using the fact that for densities between $\rho_1 = 10^{-14}$ and $\rho_{\text{sink}} = 10^{-12} \text{ g cm}^{-3}$ the gas evolves as $c \propto \rho^{1/3}$ (cf. Eqn. 1) the minimum fragment mass at ρ_1 of Eqn. 9 translates to a minimum mass of a sink at ρ_{sink} of order $0.05 M_{\odot}$ for $\mathcal{N}_{\text{neib}} \sim 100$ (Bate & Burkert 1997). Therefore, we obtain $r_{\text{sink}} \sim 20 \text{ AU}$.

Gas particles are accreted by a sink when i) they have approached the sink at a distance less than r_{sink} , and ii) they are gravitationally bound to the sink. In order to model accretion by sinks properly, a number of boundary corrections must be applied to the neighbouring gas particles of a sink, so that these gas particles do not feel a discontinuity in the density field due to the proximity of a sink. We have implemented all the boundary corrections given by Bate *et al.* (1995).

4.8.2 Results

The two protostars identified at the end of the simulation *without* sinks (Fig. 4), are replaced by sinks at $t \sim 0.391$ and $t \sim 0.393 \text{ Myr}$ (upper left panel of Fig. 9; these are the sinks on the right and in the middle of the panel, respectively). Note that the sink on the right hand side of the upper left panel of Fig. 9 lies below (lower y value) the sink in the middle of the panel (cf. the left panel of Fig. 4). As the simulation with sinks progresses, the sink on the right hand side of the upper left panel of Fig. 9 first moves to the left towards the centre of the computational domain and later it is forced to move along the z -axis by shear produced by material entering the shock compressed layer (at an angle) from the opposite side. At the time of the upper right panel of Fig. 9, this sink has exited the small field of view of this panel (from the top side).

In the meantime, a third protostar formed (cf. Section 4.3) in the top left hand corner of the displayed region and at $t \sim 0.400 \text{ Myr}$ it was replaced by a sink. At the time of the upper right panel of Fig. 9 ($t \sim 0.402 \text{ Myr}$), the two sinks remaining in the displayed region have already approached each other along the filament. They have a close encounter with periastron $\sim 200 \text{ AU}$ at $t \sim 0.403 \text{ Myr}$ and capture themselves into a binary. A large circumbinary disc forms around the binary. The binary components continue accreting matter from this disc and their orbit is hardened. At the same time, the disc material is replenished by material

falling on it from the filaments. Interactions between the accretion flows and the disc lead to the formation of further companions to the binary (see e.g. the sinks on the spiral arms of the disc in the lower panels of Fig. 9). Most of these companions are ejected within a few orbits around the binary after having a close encounter with it (e.g. the sinks in the lower density regions of the left panel of Fig. 10).

At the end of the simulation with sinks (right panel of Fig. 10, $t_{\text{evol}} \sim 2.6 t_{\text{ff}}$), the binary components have mass of $\sim 1.5 M_{\odot}$ each, and their separation is $\sim 40 \text{ AU}$, i.e. the minimum separation resolved due to the Plummer softening that is used to model sink-sink interactions. Eight additional sinks have formed in total (including a sink that has exited the displayed region; this sink has final mass of $\sim 0.5 M_{\odot}$). The masses of the secondary protostars, grouped in two mass bins, are denoted by different symbols in Fig. 11 (squares for $0.1 M_{\odot} < M < 1.0 M_{\odot}$ and triangles for $M < 0.1 M_{\odot}$). Their projected velocities are also indicated by the lines in Fig. 11. None of them remains bound to the binary. However, they have been ejected from the system with moderate velocities of order a few km s^{-1} (e.g. the object having a close encounter with the binary on the right panel of Fig. 11).

A more detailed account of the properties of this system of protostars is beyond the scope of this paper. We note, however, that the general picture drawn from our simulation with sinks with respect to the formation and evolution of this system of protostars is similar to that of one of the subclusters reported by Bate & Bonnell (2005), which has also formed along filaments. A small difference to the results of Bate & Bonnell is the lower rate with which secondaries form in our simulation, which we attribute to the stiffer equation of state used here (with polytropic exponent of 5/3 instead of 7/5 that is used by Bate & Bonnell). A stiff equation of state provides proto-fragments with larger thermal pressure support. For example, we have noted that fragments like the one in the top left hand corner of the right panel of Fig. 10 form a sink only when they fall onto the disc, i.e. when they get very quickly loaded with mass exceeding a Jeans mass. We also note that no individual discs and/or envelopes can be resolved here for any of the 10 sinks formed, i.e. if any of these protostars is attended by a disc and/or surrounded by an envelope, this disc/envelope will be smaller than $r_{\text{sink}} \sim 20 \text{ AU}$ in size. The separation of the binary is, accordingly, expected to be smaller than $\sim 40 \text{ AU}$ which is the minimum separation than can be resolved. Finally, we note that, despite the very small number statistics, the mass distribution of the sinks formed here is consistent with the observed protostellar mass distributions in several star forming regions.

The total mass in sinks at the end of the simulation is $5.1 M_{\odot}$, which implies a SFE of order 25%. There is, however, about $3 M_{\odot}$ more bound gas in the filaments, but we expect only the binary components to have access to this material. Moreover, we expect accretion onto these two protostars to start decreasing at subsequent times, i.e. when they enter the Class I phase, during which stellar feedback effects (which we do not model here) start affecting the disc from which they now accrete. We do not anticipate, therefore, more than $1\text{-}2 M_{\odot}$ of additional stellar mass in the binary and/or additional secondaries, limiting the SFE of this collision to a maximum value of $\sim 30\%$. Because this collision is one of the most efficient among the collisions we study

here, we estimate the average SFE of the low-mass clump collisions to be of order 20-30%. After having conducted the simulation with sinks, we note that, in terms of primary protostellar mass, our initial SFE estimate, which was made in the previous section by extrapolating the masses obtained from the simulations without sinks and using well known protostellar mass accretion rates and lifetimes, was rather accurate. The SFE estimate obtained from the simulation with sinks also accounts for the formation of secondary protostars, which we could not follow before introducing sinks, and has led to this higher SFE of order 20-30%.

5 $75M_{\odot}$ CLUMP COLLISIONS

In this section we present the results of the suite of three simulations involving collisions between clumps having mass $M_0 = 75M_{\odot}$. The Mach Number is set to $\mathcal{M} = 9$, and the offset parameter is set to $b = 0.2, 0.4,$ and 0.5 . The purpose of this suite of simulations is to explore how the results depend on clump mass M_0 , and to test the reliability of the results reported by Bhattal *et al.* (1998).

The main effect of increasing the clump mass, M_0 , and hence also the clump radius, R_0 , is that – at fixed b – the shock compressed layer is more extended and the fragmentation scale is also somewhat greater (*cf.* Eqn. 14). Consequently, the shock compressed layer breaks up into a more complex network of filaments, as the number of filaments should be $\propto M_0^{1/4}$.

The main conclusion concerning the simulations reported by Bhattal *et al.* (1998) is that their results are seriously corrupted, both by the fact that the Jeans condition is violated, and by the fixed (and rather large) gravity softening length.

5.1 $M_0 = 75M_{\odot}$, $b = 0.2$, $\mathcal{M} = 9$

After ~ 0.61 Myr, the shock compressed layer has become sufficiently dense and massive to break up into a network of tumbling filaments. Protostars then start to condense out at the intercepts of the filaments. On-the-Fly splitting starts at ~ 0.63 Myr. In total, four protostars form, but two of them quickly merge. The three surviving protostars are rotating rapidly, and attended by accretion discs with strong spiral structure. Because of the increasing offset between the opposing streams accreting onto a protostar along the filament, the protostellar disc is spun up, and we anticipate that the disc will eventually fragment to produce secondary companions. However, the simulation has been terminated before this happens. The accretion streams are very smooth.

In comparison with the lower-mass ($10M_{\odot}$) collision at $b = 0.2$, more filaments and more protostars are formed, because the area of the shock compressed layer is larger and the fragmentation scale L_{frag} is only moderately larger.

At the end of the simulation (~ 0.64 Myr; Figs. 12 & 13), the total mass of the three protostars is $\sim 0.85M_{\odot}$, and their radii are in the range 100 to 130 AU. Their central densities exceed ρ_1 , so they have already started to heat up adiabatically. The separation between the protostars is $\sim 10^4$ AU (Fig. 12), and they are only weakly bound, so it is almost certain that within 1 Myr one of them will be ejected gravitationally by the other two. The minimum density in the

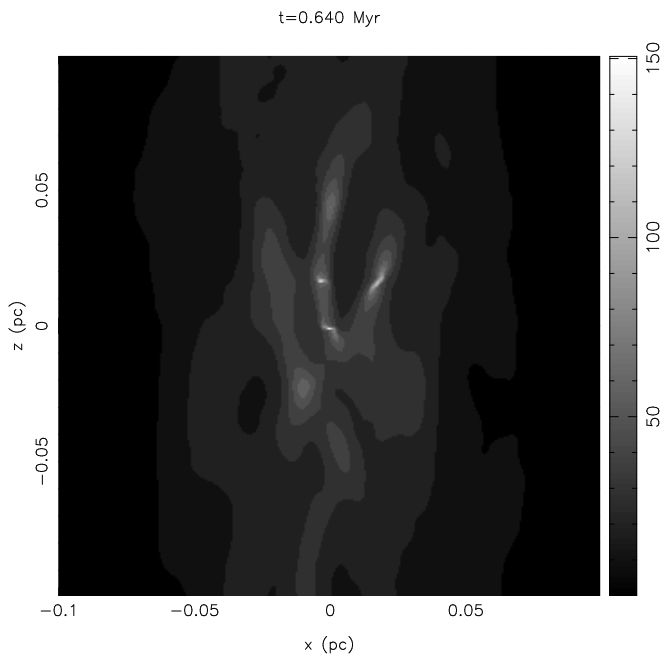


Figure 13. $M_0 = 75M_{\odot}$, $b = 0.2$, $\mathcal{M} = 9$, at the end of the simulation, ($t = 0.640$ Myr), viewed along the y -axis to show the network of filaments produced; $\Delta x = \Delta z = 0.2$ pc; sixteen-interval logarithmic grey-scale, in units of g cm^{-2} , from $7.24 \times 10^{-2} \text{ g cm}^{-2}$ to $1.51 \times 10^2 \text{ g cm}^{-2}$ ($1.81 \times 10^{22} \text{ H}_2 \text{ cm}^{-2}$ to $3.78 \times 10^{25} \text{ H}_2 \text{ cm}^{-2}$).

filaments is $\rho_{\text{fil}} \sim 3.0 \times 10^{-17} \text{ g cm}^{-3}$ ($n_{\text{H}_2} \sim 5 \times 10^6 \text{ cm}^{-3}$, Fig. 13). The number of active particles has increased from 220,000 to 260,000.

In contrast, Bhattal *et al.* (1998) found that for low- b collisions a single primary protostar formed at the centre of the collision and accreted material from a single filament. The primary protostar rapidly acquired an accretion disc, and grew in mass and angular momentum as the offset between the opposing accretion streams along the filament increased. Due to the development of spiral structure in the disc, and the lumpiness of the accretion streams, lower-mass secondary companions formed in the disc around the primary. There was no suggestion of the shock compressed layer fragmenting into multiple filaments. Moreover, the secondary companions modelled by Bhattal *et al.* were not always resolved properly, as in some cases they contained fewer than 50 particles. Also Bhattal *et al.* used a large and constant gravity softening length $\epsilon \sim 500$ AU, so that they could not resolve the formation of an object until its size became $\gtrsim 500$ AU.

We conclude that the evolution of the density field is followed more faithfully in our current simulations with Particle Splitting. The fact that the Jeans condition is obeyed, prevents a central object from forming artificially before the filaments. Also there is no preferred length scale, so we can trust the detailed evolution of the discs and their dynamical interaction with the filaments.

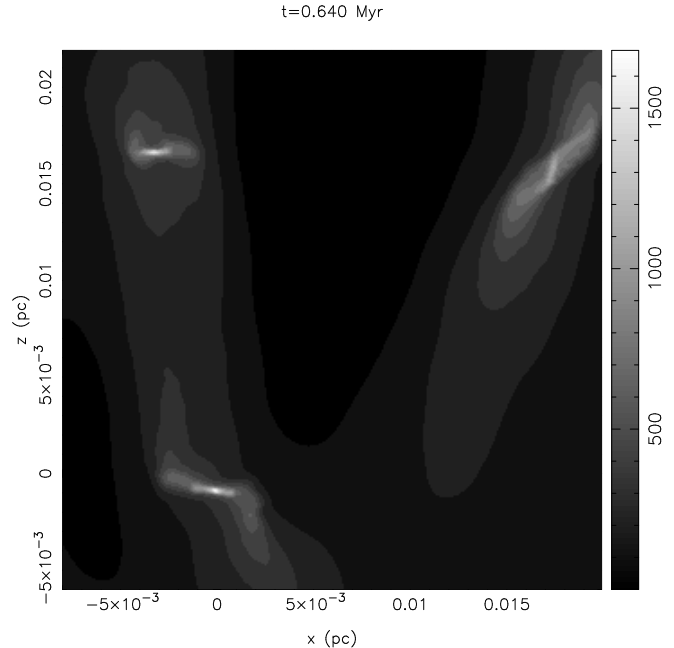


Figure 12. $M_0 = 75M_\odot$, $b = 0.2$, $\mathcal{M} = 9$, at the end of the simulation, ($t = 0.640$ Myr). *Left Panel.* View along the z -axis; $\Delta x = 0.04$ pc, $\Delta y = 0.08$ pc; sixteen-interval logarithmic grey-scale, in units of g cm^{-2} , from $3.63 \times 10^{-2} \text{ g cm}^{-2}$ to $7.59 \times 10^2 \text{ g cm}^{-2}$ ($9.08 \times 10^{21} \text{ H}_2 \text{ cm}^{-2}$ to $1.90 \times 10^{26} \text{ H}_2 \text{ cm}^{-2}$). *Right Panel.* View along the y -axis; $\Delta x = \Delta z = 0.028$ pc; sixteen-interval logarithmic grey-scale, in units of g cm^{-2} , from $2.00 \times 10^{-1} \text{ g cm}^{-2}$ to $1.70 \times 10^3 \text{ g cm}^{-2}$ ($5.00 \times 10^{22} \text{ H}_2 \text{ cm}^{-2}$ to $4.25 \times 10^{26} \text{ H}_2 \text{ cm}^{-2}$).

5.2 $M_0 = 75M_\odot$, $b = 0.4$, $\mathcal{M} = 9$

A single tumbling filament forms at ~ 0.66 Myr. On-the-Fly Particle Splitting starts at about the same time. At least four protostars condense out of the filament; a further two may have started to condense out.

At the end of the simulation (~ 0.686 Myr; Fig. 14), the total mass of the four well established protostars is $\sim 0.40M_\odot$. They are positioned randomly along the filament, and they are falling towards one another. The most massive protostar is disc-like with a radius of ~ 170 AU (Fig. 14). The three smaller protostars are still roughly spherical with radii ~ 45 AU. Their central densities exceed ρ_1 , so they have started heating up adiabatically. The number of active particles has increased from 220,000 to 260,000.

This is very similar to what happened in the corresponding simulation performed by Bhattal *et al.* (1998), except that their simulation was followed further, and the disc round the most massive protostar was therefore spun up by accretion along the tumbling filament. As a consequence it became rotationally unstable, and fragmented to produce secondary companions. This might also have happened here, if we had been able to follow the simulation for long enough. However, once again we can have little faith in the Bhattal *et al.* result because some of the secondaries contained at their inception less than 50 particles, and gravity was severely softened on scales $\lesssim 500$ AU.

5.3 $M_0 = 75M_\odot$, $b = 0.5$, $\mathcal{M} = 9$

On-the-Fly Particle Splitting starts at ~ 0.72 Myr. At ~ 0.73 Myr, a single tumbling filament forms, and fragments

into several protostars. Two of them, at the bottom right hand corner of Fig. 15, condense out first and eventually, at ~ 0.746 Myr, they merge. Subsequently, another three protostars form, two near the centre of the filament and one at the left hand end (Fig. 15). All fragments remain spherical and are strongly centrally condensed. Some other density enhancements appear in the filament, suggesting that more fragments may be forming.

At the end of the simulation (~ 0.75 Myr), the total mass of the four well established protostars is $\sim 0.65M_\odot$. The most massive one has radius ~ 35 AU and the radii of the other three are ~ 100 AU. Their central densities exceed ρ_1 , so they have started to heat up adiabatically. The minimum density in the filament is $\rho_{\text{fil}} \sim 2 \times 10^{-18} \text{ g cm}^{-3}$ ($n_{\text{H}_2} \sim 5 \times 10^5 \text{ cm}^{-3}$). The number of active particles has increased from 220,000 to 342,000.

Again, this is very similar to what happened in the corresponding simulation performed by Bhattal *et al.* (1998), where a single tumbling filament formed and then fragmented. Bhattal *et al.* performed a standard resolution simulation of this case, which produced two protostars after ~ 1 Myr, and a higher-resolution simulation in which each component of the binary was itself a binary, i.e. an hierarchical quadruple.

5.4 Discussion of $75M_\odot$ collisions

In the $b = 0.2$ collision, the shock compressed layer has considerable lateral extent, and fragments into a network of tumbling filaments; multiple protostars then condense out of these filaments. In the $b = 0.4$ and $b = 0.5$ collisions, the extent of the shock compressed layer is considerably smaller,

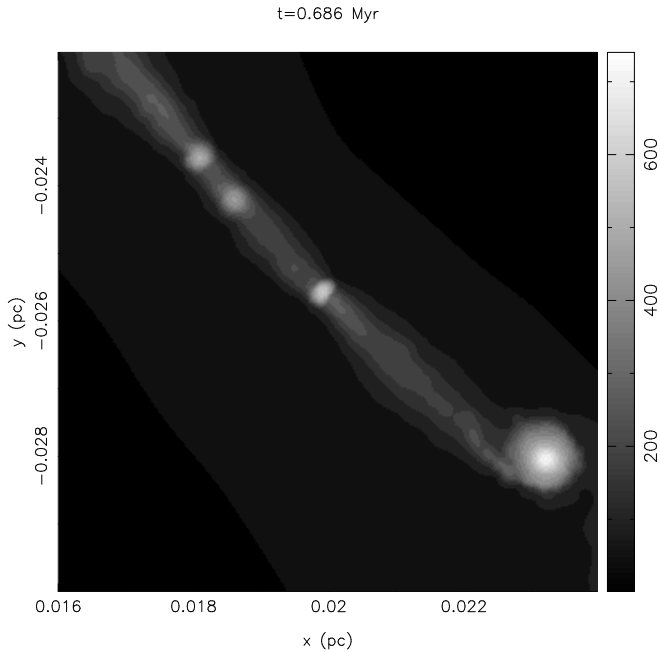


Figure 14. $M_0 = 75M_\odot$, $b = 0.4$, $\mathcal{M} = 9$, at the end of the simulation ($t = 0.686$ Myr), viewed along the z -axis; $\Delta x = \Delta y = 0.008$ pc; sixteen-interval logarithmic grey-scale, in units of g cm^{-2} , from $9.33 \times 10^{-1} \text{ g cm}^{-2}$ to $7.41 \times 10^2 \text{ g cm}^{-2}$ ($2.33 \times 10^{23} \text{ H}_2 \text{ cm}^{-2}$ to $1.85 \times 10^{26} \text{ H}_2 \text{ cm}^{-2}$).

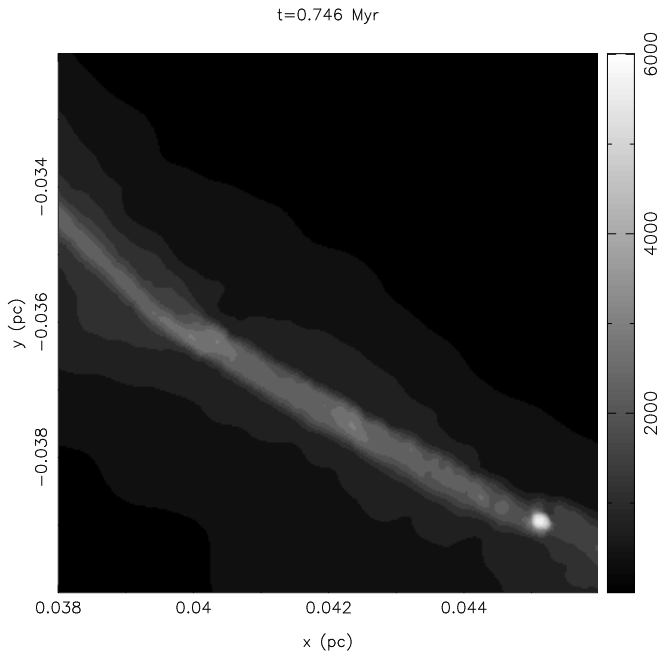


Figure 15. $M_0 = 75M_\odot$, $b = 0.5$, $\mathcal{M} = 9$ at the end of the simulation ($t = 0.750$ Myr), viewed along the z -axis; $\Delta x = \Delta y = 0.008$ pc; sixteen-intervals logarithmic grey-scale, in units of g cm^{-2} , from $3.98 \times 10^{-1} \text{ g cm}^{-2}$ to $6.03 \times 10^3 \text{ g cm}^{-2}$ ($9.95 \times 10^{22} \text{ H}_2 \text{ cm}^{-2}$ to $1.51 \times 10^{27} \text{ H}_2 \text{ cm}^{-2}$).

and in the first instance it produces a single tumbling filament, which then fragments into a line of protostars. As these protostars accrete material with increasing specific angular momentum from the tumbling filament, accretion discs form around them and develop spiral structure. At the same time the protostars fall towards one another, and they are therefore likely to interact, either merging, being captured into binary systems, or triggering the formation of further protostars.

The main difference between the $10M_\odot$ collisions of Section 4, and the $75M_\odot$ collisions of this section, is that the latter involve more mass *and* produce a shock compressed layer of greater extent. Consequently the filaments are longer and spawn more protostars, typically 4 to 6 (as compared with 1 to 2 for the $10M_\odot$ collisions). Despite the fragmentation scale being somewhat larger, there tend to be more filaments, at least for low- b collisions.

Taking into account that in the $75M_\odot$ collisions i) there are on average three times more primary protostars than in the $10M_\odot$ collisions, and ii) there is more mass available for protostars to accrete in the shock compressed layer (and thus also in the filaments), and using the SFE estimated in Section 4.8 for the $10M_\odot$ collisions, we arrive to an average SFE estimate of order 10-15% for the $75M_\odot$ collisions (as the total available gas mass is 7.5 times larger).

It seems inescapable that the results obtained by Bhattal *et al.* (1998) were corrupted, both by the very large gravity smoothing length, and by the fact that the Jeans condition was violated (i.e. the Jeans mass was not resolved at all times). The inferences which they made are therefore not reliable.

6 CONCLUSIONS

We have conducted a series of simulations of star formation triggered by low-velocity collisions between low-mass molecular clumps. By implementing On-the-Fly Particle Splitting in these simulations, we have ensured that the Jeans condition is satisfied throughout the computational domain, at all times. Consequently we are confident that our simulations have not been corrupted by artificial fragmentation, and that real fragmentation has not been inhibited by inadequate resolution. We are therefore now in a position to apply our SPH code with Particle Splitting to simulations of clump-clump collisions with more realistic initial conditions, for example clumps of unequal mass, clumps with internal turbulence, and/or rotating clumps. The use of Particle Splitting will afford significant advantages in terms of computational efficiency.

In order to confirm the usefulness and reliability of this technique, we have repeated the $M_0 = 10M_\odot$, $b = 0.2$, $\mathcal{M} = 10$ simulation, using a standard code without Particle Splitting, but introducing less massive (13 times less massive) particles, from the outset, and 13 times as many of them (i.e. 390,000 particles in total). The results differ only in small details, not in the overall statistics of fragmentation, such as the number and mass of the protostars formed. Moreover, the standard simulation with 390,000 particles uses ~ 6 times more memory, and ~ 2 times more CPU than the simulation using On-the-Fly Particle Splitting with only 30,000 particles initially.

The simulations presented here demonstrate that the primary mode creating protostars, following a clump-clump collision, entails the formation of a shock compressed layer (while the gas is cooling radiatively), its gravitational fragmentation into one or more filaments (the number depending on the lateral extent of the layer and the fragmentation scale), the break up of the filaments into cores, the condensation of primary protostars out of the cores, and the subsequent growth of the protostars by accretion along the filaments. Similar filamentary structures and cores have been found in the simulations of Pongracic *et al.* (1992), Klessen & Burkert (2000; 2001), Klessen (2001), Bate *et al.* (2002a; 2002b; 2003), Bate & Bonnell (2005), Jappsen *et al.* (2005), Martel, Evans & Shapiro (2006).

Increasing the clump mass M_0 (with b and \mathcal{M} held constant) increases the number of primary protostars, because the mass and lateral extent of the shock compressed layer is greater, and the fragmentation scale L_{frag} is only moderately larger. Increasing b (with M_0 and \mathcal{M} held constant) reduces the number of primary protostars, because the lateral extent of the shock compressed layer is reduced (and the fragmentation length is increased somewhat by shear). Increasing b also increases the orbital angular momentum of the resulting ensemble of protostars. Increasing \mathcal{M} (with M_0 and b held constant) increases the number of primary protostars because it reduces L_{frag} . It also increases the orbital angular momentum of the resulting ensemble of protostars.

For collisions with $b \gtrsim 0.6$, no significant shock compressed layer forms, and the clump-clump collision does not trigger star formation. For collisions with $b \lesssim 0.5$, the filaments and cores that form have densities $n_{\text{H}_2} \gtrsim 10^5 \text{ cm}^{-3}$. Therefore it should be possible to map them in NH_3 or CS, in nearby star formation regions. The protostars which condense out of a core have much higher central densities $n_{\text{H}_2} \gtrsim 10^{10} \text{ cm}^{-3}$. Material accretes onto the protostars at rates in the range 1 to $5 \times 10^{-5} M_{\odot} \text{ yr}^{-1}$, and this lasts for a time interval in the range 1 to 3×10^4 yrs. Therefore we should identify these protostars with the Class 0 phase of evolution (Lada 1999).

Hartmann (2002) has recently pointed out that young stars in Taurus form primarily within gaseous filaments, via fragmentation of the filaments; that the mean separation between the young stars in Taurus is of order the local Jeans length; and that the protostellar cores are elongated along the filaments. This is very similar to the phenomenology which we observe in our simulations. In our simulations, the shock compressed layer created by the clump-clump collision fragments into filaments, and the filaments then fragment into cores; the separations between cores are of order the local Jeans length; and the individual cores are prolate and elongated parallel to the filaments. Our findings on filament fragmentation derived from clump-clump collision simulations agree with those of Jappsen *et al.* (2005) obtained from simulations of the turbulent ISM. They also fit the theoretical predictions of Larson (2005) on the fragmentation of filaments and the influence of thermodynamics.

The prolateness of the cores in our simulations is only evident from the grey-scale plots we have presented, if one takes into account that molecular-line observations tend to be most sensitive to gas at the corresponding critical density ($\sim 10^3 \text{ cm}^{-3}$ to $\sim 10^5 \text{ cm}^{-3}$, for the lines used to map cores in Taurus), and submillimeter observations are opti-

cally thick for column-densities exceeding $4 \times 10^{25} \text{ H}_2 \text{ cm}^{-2}$. In other words one must look at the grey contours to see the structures which would be revealed by molecular-line or submillimeter continuum observations. Therefore, whereas the protostellar discs formed in our simulations present a range of shapes (dependent on whether they are viewed close to edge-on or close to pole-on), the cores within which these discs are embedded are almost invariably prolate and elongated along the filament from which they are condensing. The elongation along the filament arises because the cores are usually being fed by two opposing accretion streams from along the filament.

Because the filaments are tumbling, the accretion flow onto a protostar tends to deliver ever increasing specific angular momentum, and therefore the protostar is spun up. This may lead to rotational instabilities which create secondary companions to the primary protostars. However, the simulations have been terminated (due to limited computational resource) before there is any clear evidence of this happening.

Additionally, protostars condensing out of the same filament will often fall together, and therefore they may interact. Ultimately, this could result in a merger, or in capture to form a binary, or in further fragmentation to produce secondary protostars, but again we have not followed the simulations for that long. The temptation is to introduce sink particles, but then the interaction is not properly modelled, because of the over-simplifications associated with the introduction of and the interaction between sink particles. Nevertheless, we have repeated one of the low-mass clump collision simulations using sink particles. This attempt has shown that, indeed, pairs of primary protostars can form close binaries through capture, as they move towards each other along a tumbling filament. It has also been shown that such binaries can be attended by massive circumbinary discs and that the formation of secondary companions to such a binary is possible through the interaction of its disc with the accretion flows onto it from along the filament.

The SFE of low-mass clump collisions is estimated to be of order 20-30% based on the result of the simulation with sinks. We have asserted that the SFE decreases with increasing mass and, in particular, that the SFE of the $75M_{\odot}$ collisions is of order 10-15%. Both these values are in accordance with the findings of Hunter *et al.* (1986) from simulations of colliding gas flows. The SFEs estimated from our simulations are also consistent with those (20-30%) observed in a number of molecular clouds (Rengarajan 1984), which implies that clump-clump collisions can account, at least partly, for the star formation in those molecular clouds that can provide this triggering mechanism.

Taken at face value, the above (theoretical and observational) estimates for the SFE could be interpreted in the following sense: in the absence of any other triggering mechanism, star formation in the ISM can be attributed mainly to low-mass clump collisions and not to collisions between higher-mass clumps. Evidently, this is not true in nature: first, these SFE estimates are only meaningful in a statistical sense, i.e. there is great variation from region to region; second, there is a number of complementary and/or mutually excluding mechanisms that are simultaneously in play. Collisions between low-mass clumps (and/or small-scale shocks produced in the turbulent ISM as part of larger-scale collid-

ing flows) appear to be one such mechanism able to explain part of the star formation observed in the Galaxy.

Further progress will probably also necessitate simulations at even higher resolution, e.g. by employing multiple levels of particle splitting and using smaller sink particles (Kitsionas *et al.*, in prep.). The detailed study of discs will also require the introduction of a more sophisticated algorithm to regulate the shear viscosity, for instance by using the time-dependent formulation of Morris & Monaghan (1997) and/or the Balsara (1995) switch, the implementation of a realistic continuity equation advocated by Imaeda & Inutsuka (2002) (despite the recent criticism by Monaghan (2006) of the need of the latter formalism), and possibly all these should be attempted in combination with a different method for the velocity calculation, such as XSPH (Monaghan 2002).

ACKNOWLEDGEMENTS

The authors thank the anonymous first referee for useful and constructive comments and especially for his/her suggesting of the implementation of sink particles in our SPH code with particle splitting. They also thank the second referee, Ralf Klessen, for his comments and suggestions as well as Simon Glover for proof reading the manuscript. The authors are thankful to Simon Goodwin, Henri Boffin and Neil Francis for many interesting discussions on this project as well as for their assistance on the implementation of sinks. They acknowledge the use of the Sun E4000 computer of the Cardiff Centre for Computational Science and Engineering as well as Sun workstations at both the School of Physics & Astronomy, Cardiff University and the Institute of Astronomy & Astrophysics, National Observatory of Athens. They also acknowledge the use of the public visualisation tool “Super-SPHplot” developed by Daniel Price. For part of the work presented in this paper, SK kindly acknowledges support by an EU Commission “Marie Curie Intra-European (Individual) Fellowship” of the 6th Framework Programme. Finally, SK would like to dedicate this paper to the memory of his school-time friend Dimitrios Velenis.

REFERENCES

- Balsara D. S., 1995, *JCP*, **121**, 357
 Barnes J., Hut P., 1986, *Nature*, **324**, 446
 Bate M. R., Bonnell I. A., 2005, *MNRAS*, **356**, 1201
 Bate M. R., Burkert A., 1997, *MNRAS*, **288**, 1060
 Bate M. R., Bonnell I. A., Bromm V., 2002a, *MNRAS*, **332**, L65
 Bate M. R., Bonnell I. A., Bromm V., 2002b, *MNRAS*, **336**, 705
 Bate M. R., Bonnell I. A., Bromm V., 2003, *MNRAS*, **339**, 577
 Bate M. R., Bonnell I. A., Price N. M., 1995, *MNRAS*, **277**, 362
 Bergin E. A., Hartmann L. W., Raymond J. C., Ballesteros-Paredes J., 2004, *ApJ*, **612**, 921
 Bhattal A. S., Francis N., Watkins S. J., Whitworth A. P., 1998, *MNRAS*, **297**, 435
 Bonnor W. D., 1956, *MNRAS*, **116**, 351
 Boss A. P., Bodenheimer P., 1979, *ApJ*, **234**, 289
 Chapman S., Pongracic H., Disney M., Nelson A., Turner J., Whitworth A., 1992, *Nature*, **359**, 207
 Crutcher R. M., Nutter D. J., Ward-Thompson D., Kirk J. M., 2004, *ApJ*, **600**, 279
 Ebert R., 1955, *ZA*, **37**, 217
 Gingold R. A., Monaghan J. J., 1977, *MNRAS*, **181**, 375
 Greaves J. S., White G. J., 1991, *A&A*, **248**, L27
 Hartmann L., 2002, *ApJ*, **578**, 914
 Hasegawa T., Sato F., Whiteoak J. B., Miyawaki R., 1994, *ApJ*, **429**, L77
 Hernquist L., Katz N., 1989, *ApJS*, **70**, 419
 Hunter J. H., Sandford M. T., Whitaker R. W., Klein R. I., 1986, *ApJ*, **305**, 309
 Imaeda Y., Inutsuka S., 2002, *ApJ*, **569**, 501
 Inutsuka S., Miyama S. M., 1992, *ApJ*, **388**, 392
 Jappsen A.-K., Klessen R. S., Larson R. B., Li Y., Mac Low M.-M., 2005, *A&A*, **435**, 611
 Kitsionas S., 2000, PhD Thesis, University of Wales (*astro-ph/0307478*)
 Kitsionas S., Whitworth A. P., 2002, *MNRAS*, **330**, 129
 Klein R. I., Fisher R. T., McKee C. F., Truelove J. K., 1999, in Miyama S. M., Tomisaka K., Hanawa T., eds, *Astrophysics and space science library vol. 240, Numerical Astrophysics*. Kluwer Academic, Boston, p. 131
 Klessen R. S., 2001, *ApJ*, **556**, 837
 Klessen R. S., Burkert A., 2000, *ApJS*, **128**, 287
 Klessen R. S., Burkert A., 2001, *ApJ*, **549**, 386
 Lada C. J., 1999, in Lada C. J., Kylafis N. D., eds, *NATO Science Series, The Origin of Stars and Planetary Systems*. Kluwer Academic Publishers, p. 143
 Larson R. B., 1981, *MNRAS*, **194**, 809
 Larson R. B., 2005, *MNRAS*, **359**, 211
 Lucy L. B., 1977, *AJ*, **82**, 1013
 Mac Low M.-M., Klessen R. S., 2004, *Rev. Mod. Phys.*, **76**, 125
 Marinho E. P., Lépine J. R. D., 2000, *A&AS*, **142**, 165
 Marinho E. P., Andreazza C. M., Lépine J. R. D., 2001, *A&A*, **379**, 1123
 Martel H., Evans N. J. I., Shapiro P. R., 2006, *ApJS*, **163**, 122
 Miyawaki R., Hayashi M., Hasegawa T., 1999, in Nakamoto T., ed., *Star Formation 99*, p. 379
 Monaghan J. J., 1992, *Ann. Rev. A&A*, **30**, 543
 Monaghan J. J., 2002, *MNRAS*, **335**, 843
 Monaghan J. J., 2005, *Rep. Prog. Phys.*, **68**, 1703
 Monaghan J. J., 2006, *MNRAS*, **365**, 199
 Monaghan J. J., Lattanzio J. C., 1985, *A&A*, **149**, 135
 Morris J. P., Monaghan J. J., 1997, *JCP*, **136**, 41
 Padoan P., Nordlund A., 2002, *ApJ*, **576**, 870
 Pongracic H., Chapman S. J., Davies J. R., Disney M. J., Nelson A. H., Whitworth A. P., 1992, *MNRAS*, **256**, 291
 Rengarajan T. N., 1984, *ApJ*, **287**, 671
 Sato F., Hasegawa T., Whiteoak J. B., Miyawaki R., 2000, *ApJ*, **535**, 857
 Scalo J. M., 1985, in Black D. C., Matthews M. S., eds, *Protostars and Planets II*. Univ. Arizona Press, Tucson, p. 201
 Scoville N. Z., Sanders D. B., Clemens D. P., 1986, *ApJ*, **310**, L77
 Stutzki J., Güsten R., 1990, *ApJ*, **356**, 513
 Tan J. C., 2000, *ApJ*, **536**, 173
 Tohline J. E., 1982, in Canuto V. M., Elmegreen B. G., eds, *Fundamentals of cosmic physics vol. 8*. Gordon and Breach Science Publishers, p. 1
 Truelove K. J., Klein R. I., McKee C. F., Holliman J. H., Howell L. H., Greenough J. A., 1997, *ApJ*, **489**, L179
 Truelove K. J., Klein R. I., McKee C. F., Holliman J. H., Howell L. H., Greenough J. A., Woods D. T., 1998, *ApJ*, **495**, 821
 Turner J. A., Chapman S. J., Bhattal A. S., Disney M. J., Pongracic H., Whitworth A. P., 1995, *MNRAS*, **277**, 705
 Vazquez-Semadeni E., Kim J., Ballesteros-Paredes J., 2005, *ApJ*, **630**, L49
 Vazquez-Semadeni E., Kim J., Shadmehri M., Ballesteros-Paredes J., 2005, *ApJ*, **618**, 344
 Whitworth A. P., 1998, *MNRAS*, **296**, 442
 Whitworth A. P., Clarke C. J., 1997, *MNRAS*, **291**, 578

- Whitworth A. P., Boffin H. M. J., Francis N., 1998, *MNRAS*, **299**, 554
- Whitworth A. P., Bhattal A. S., Chapman S. J., Disney M. J., Turner J. A., 1994a, *A&A*, **290**, 421
- Whitworth A. P., Bhattal A. S., Chapman S. J., Disney M. J., Turner J. A., 1994b, *MNRAS*, **268**, 291
- Whitworth A. P., Chapman S. J., Bhattal A. S., Disney M. J., Pongracic H., Turner J. A., 1995, *MNRAS*, **277**, 727
- Williams J. P., de Geus E. J., Blitz L., 1994, *ApJ*, **428**, 693

This figure "kitsionas_fig2.jpg" is available in "jpg" format from:

<http://arxiv.org/ps/astro-ph/0703177v1>

This figure "kitsionas_fig3a.jpg" is available in "jpg" format from:

<http://arxiv.org/ps/astro-ph/0703177v1>

This figure "kitsionas_fig4a.jpg" is available in "jpg" format from:

<http://arxiv.org/ps/astro-ph/0703177v1>

This figure "kitsionas_fig12a.jpg" is available in "jpg" format from:

<http://arxiv.org/ps/astro-ph/0703177v1>